

Electronic Theses and Dissertations, 2004-2019

2010

Vaporization Characteristics Of Pure And Blended Biofuel Droplet Injected Into Hot Stream Of Air

Abhishek Saha
University of Central Florida

 Part of the [Mechanical Engineering Commons](#)
Find similar works at: <https://stars.library.ucf.edu/etd>
University of Central Florida Libraries <http://library.ucf.edu>

This Masters Thesis (Open Access) is brought to you for free and open access by STARS. It has been accepted for inclusion in Electronic Theses and Dissertations, 2004-2019 by an authorized administrator of STARS. For more information, please contact STARS@ucf.edu.

STARS Citation

Saha, Abhishek, "Vaporization Characteristics Of Pure And Blended Biofuel Droplet Injected Into Hot Stream Of Air" (2010). *Electronic Theses and Dissertations, 2004-2019*. 4422.
<https://stars.library.ucf.edu/etd/4422>



University of
Central
Florida

STARS
Showcase of Text, Archives, Research & Scholarship

VAPORIZATION CHARACTERISTICS OF PURE AND BLENDED BIOFUEL DROPLET
INJECTED INTO HOT STREAM OF AIR

by

Abhishek Saha
B.S., Jadavpur University, India, 2006

A thesis submitted in partial fulfillment of the requirements
for the degree of Master in Science in Mechanical Engineering
in the department of Mechanical, Materials and Aerospace Engineering
in the College of Engineering and Computer Science
at the University of Central Florida
Orlando, Florida

Summer Term
2010

© 2010 Abhishek Saha

ABSTRACT

The combustion dynamics and stability are dependent on the quality of mixing and vaporization of the liquid fuel in the pre-mixer. The vaporization characteristics of different blends of biofuel droplets injected into the air stream in the pre-mixer are modeled in this current study. The focus of this work is on the blended alternate fuels which are lately being considered for commercial use. Two major alternate fuels analyzed are ethanol and Rapeseed Methyl Esters (RME). Ethanol is being used as a substitute for gasoline, while RME is an alternative for diesel. In the current work, the vaporization characteristics of a single droplet in a simple pre-mixer has been studied for pure ethanol and RME in a hot air jet at a temperature of 800 K. In addition, the behavior of the fuels when they are mixed with conventional fuels like gasoline and diesel is also studied. Temperature gradients and vaporization efficiency for different blends of bio-conventional fuel mixture are compared with one another. The model was validated using an experiment involving convection heating of acoustically levitated fuel droplets and IR-thermography to visualize and quantify the vaporization characteristics of different biofuel blends downstream of the pre-mixer. Results show that the 20 μm droplets of ethanol-gasoline 50-50 blend is completely evaporated in 1.1 msec, while 400 μm droplets vaporized only 65% in 80 msec. In gasoline-ethanol blends, pure gasoline is more volatile than pure ethanol. In spite of having higher vapor pressure, ethanol vaporizes slowly compared to gasoline, due to the fact that latent heat of vaporization is higher for ethanol. For gasoline-ethanol blended fuels, ethanol component vaporizes faster. This is because in blended fuels gasoline and ethanol attain the same temperature and ethanol vapor pressure is higher than that for gasoline. In the case of RME-diesel blends, initially diesel

vaporizes faster up to 550K, and above this temperature, vapor pressure of RME becomes dominant resulting in faster vaporization of RME.

Current work also looks into the effect of non-volatile impurities present in biofuels. Depending on source and extraction process, fuels carry impurities which impact vaporization process. In this work these effects on ethanol blended fuel have been studied for different concentration of impurities. The presence of non-volatile impurities reduces the vaporization rate by reducing the mass fraction of the volatile component at the surface. However, impurities also increase the surface temperature of the droplet.

Finally, the effects of hot and cold spots in the prevaporizer have been investigated. Due to inefficient design, prevaporizer may have local zones where the temperature of air increases or decreases very sharply. Droplets going through these abnormal temperature zones would vaporize at a different rate than others. Current study looks into these droplets to understand the vaporization pattern.

ACKNOWLEDGMENTS

At the beginning, I would like to show my deepest appreciation to my advisors Dr. Ranganathan Kumar and Dr Saptarshi Basu, who offered me their invaluable guidance and opportunities. It is an honor for me to work with you. Without your constant advice and technical inputs this thesis would not have been completed.

I would also like to thank Dr Louis Chow, my other committee member for his thoughts and inputs on my thesis. I am also grateful to other professors of my department who helped me with their timely suggestions and knowledge sharing through different courses.

I am indebted to many of my colleagues for extending their helps and expertise, without which my research would not have been completed. Finally, I would thank my parents and friends who provided their moral support from the beginning. Their continuous encouragement has fetched me this far to complete my degree.

TABLE OF CONTENTS

List of Figures	viii
List of Tables	x
Nomenclature	xi
Chapter One: Introduction	1
Chapter Two: Theory and Model.....	4
Chapter Three: Experimental Set up.....	11
Chapter Four: Results and Discussions.....	14
Validation of Numerical results with Experiments.....	17
Validation for the case of bi-component blends	23
Computational Results in the Premixer	25
a) Comparative studies of blended fuels:.....	25
i) Ethanol-gasoline blends:	25
400 μm droplet.....	25
20 μm droplet.....	31
ii) RME Diesel Blends	33
400 μm droplet.....	33
20 μm droplet.....	39

b) Effect of Knudsen Number.....	40
c) Effect of non volatile impurities	41
d) Effect of hot and cold zones in pre-mixer	43
Chapter Five: Conclusion	47
References.....	49

LIST OF FIGURES

Figure 1: Experimental setup	11
Figure 2: Vapor pressures of different fuels	17
Figure 3: Sample image processing: Temperature distribution along the linear zone of interest. Inset: Sampled zone of interest in a water droplet after 1 sec of heating.	18
Figure 4: IR images showing droplet size reduction and surface temperature variation for four different fuel blends at different time instants. a) water and ethanol, b) gasoline and gasoline-ethanol (50-50).....	20
Figure 5: 800 μm droplets of different species; a) diameter reduction (D_0 is initial diameter, 800 μm) b)droplet surface temp evolution (D_0 is initial diameter, 800 μm).	21
Figure 6: Temperature and Ethanol mass fraction profiles in a droplet 6.5 msecs after the start of the heating process; a) Maqua et al [19] b) Current work. Initial diameter is 130 μm	24
Figure 7: 400 μm droplets of different fuel blends a) diameter reduction (D_0 is initial diameter, 400 μm) and b) surface temperature (in K) variation	27
Figure 8: Surface concentration (mass fraction) variation with time for 400 μm droplet; Ethanol-Gasoline blends.....	28
Figure 9: a) Temperature b) Ethanol concentration distributions at two time instants for ethanol-gasoline blended droplets (initial diameter 400 μm).	30
Figure 10: 20 μm droplets of different fuel blends a) diameter (D_0 is initial diameter, 20 μm) reduction and b) surface temperature (in K) variation.....	32
Figure 11: 400 μm droplets of different RME-diesel fuel blends a) diameter (D_0 is initial diameter, 400 μm) reduction and b) surface temperature (in K) variation	34

Figure 12: Surface concentration (mass fraction) variation with time for 400 μm droplets (RME-Diesel blends).....	35
Figure 13: a) Temperature b) RME concentration distributions at two time instants for RME-Diesel droplets (initial diameter 400 μm).....	37
Figure 14: 20 μm droplets of different RME-diesel fuel blends a) diameter (D_0 is initial diameter, 20 μm) reduction, b) surface temperature (in K) variation and c) Surface concentration (mass fraction of RME).....	38
Figure 15: For 20 μm ethanol droplets with different impurity level a) diameter (D_0 is initial diameter, 20 μm) and b) surface temperature (in K) variation	41
Figure 16: location and temperature of the hot and cold zones used for current work.....	44
Figure 17: Variation of surface Temperature, Diametric reduction (D/D_0) and surface concentration of RME for a 400 μm RME-diesel (50-50) droplet with the presence of hot-cold zones and without hot-cold zones (base-line).....	45

LIST OF TABLES

Table 1: RME-Diesel blends.....	15
Table 2: Ethanol-Gasoline blends.....	15
Table 3: properties of pure fuel.....	16

NOMENCLATURE

- $\underline{B}_{Mglobal}$ Overall Spalding mass transfer number
- \underline{B}_T Spalding heat transfer number
- \underline{C}_D Droplet drag coefficient
- \underline{C}_F Skin friction coefficient
- $\underline{D}_{i\infty}$ Mass diffusivity of vapor phase of 'i'th species into air
- \underline{h}_{fg} Latent heat of vaporization of the liquid
- \underline{Le}_L Lewis number of the liquid phase
- \dot{m}_i Mass flow-rate of 'i'th species at the droplet surface due to vaporization
- \dot{m} Total mass flow-rate at the droplet surface due to vaporization
- \underline{Nu}_o Nusselt number for a non-vaporizing sphere
- \underline{Nu}^* Nusselt number corrected for surface blowing effect
- \underline{Pe}_L Peclet number calculated based on liquid properties, $\underline{Pe}_L = RePr$
- \underline{Pr} Prandtl Number
- \underline{Q}_L Heat transfer into the liquid
- \underline{r} Radial coordinate in the droplet calculations

r_0	Initial droplet radius
r_s	Instantaneous droplet radius
\bar{r}_s	Non-dimensional droplet radius, $\bar{r}_s = r_s / r_0$
Re	Reynolds number of the droplet in the hot air
Sh_0	Sherwood number for a porous sphere
Sh^*	Sherwood number corrected for surface blowing effect
t	Time
\bar{T}	Non-dimensional temperature, $\bar{T} = (T - T_0) / T_0$
T_0	Initial temperature of the droplet
T_s	Droplet surface temperature
T_∞	Air temperature at far field
U	Droplet velocity in axial direction
U_s	Velocity of the circulating liquid at the droplet surface
U_∞	Air velocity at far field
V	Droplet velocity in the traverse direction
V_r	Radial component of the circulation velocity

\bar{v}_r Non-dimensional radial component of the circulation velocity, $\bar{V}_r = V_r / U_s$

\underline{V}_θ Angular component of the circulation velocity

\bar{v}_θ Non-dimensional angular component of the circulation velocity, $\bar{V}_\theta = V_\theta / U_s$

$\underline{\alpha}_L$ Thermal diffusivity of the liquid phase

β Non-dimensional surface regression rate parameter, $\beta = 1/2(\partial \bar{r}_s / \partial \tau)$

$\chi_{v,s}$ Mass fraction of the vapor phase at the droplet surface

$\chi_{v,\infty}$ Mass fraction of the vapor phase at far field

χ_i Mass fraction of 'i' th species

$\bar{\chi}_i$ Normalized mass fraction for 'i' species,

$$\bar{\chi}_i = (\chi_i - \chi_{i,o}) / \chi_{i,o}$$

$\chi_{i,o}$ Initial mass fraction of 'i' th species.

η Non-dimensional radial coordinate, $\eta = r/r_s$

$\underline{\mu}_g$ Average dynamic viscosity of air field

$\underline{\mu}_L$ Dynamic viscosity of the liquid phase

θ Angular coordinate in the droplet calculations

ρ_s Density of the vapor phase

ρ_L Density of the liquid phase

ρ_∞ Air density at far field

τ Non-dimensional time, $\tau = \alpha_L \cdot t / r_o^2$

CHAPTER ONE: INTRODUCTION

Use of alternate fuels for power generation is considered to be one of the possible solutions to power crisis. Use of biofuels as alternate fuel helps the environment by reducing the fossil fuel usages and by conserving the agricultural activity where food production is being reduced. Many of the power generation industries have already taken steps in using renewable green energy. The aero-propulsion industry has already planned to switch to 50% bio-blended fuel before year 2011. However, there exists a strong disagreement among the researchers about the effects of these bioblends on engine performances. This is principally due to the fact that the extraction process of biofuel from raw vegetable oil is still problematic [1].

The research efforts in the field of power energy generation showed that efficiency of the power generation unit depends very intimately on the fuel injection system. The working procedure of fuel injection system is based on the vaporization and dispersion characteristics of the liquid fuel. So it is obvious that the efficient design of injection system for different bio fuels for energy sector is dependent on the vaporization and dispersion processes of bio fuels. In the Lean Premixed Pre-vaporized (LPP) combustion, a homogenous lean fuel–air mixture needs to be delivered to the primary zone, and combustion has to occur at lower temperatures with leaner equivalence ratios for reduced NO_x emission. Hence for biofuel, the delivery of homogeneous mixture of fuel and air is crucial which requires a clear understanding of the vaporization characteristics of the different blends.

In a standard power generation unit, fuel is generally injected into a hot stream of air in a mixing chamber prior to entering the combustor. The fuel is sprayed into the air stream in form of droplets. Injected droplets are entrained into the high temperature air stream which undergo evaporation resulting in droplet diameter reduction and rise in droplet temperature. The entrained droplet also is transported towards the combustor side situated downstream of the injector. The heat transfer from the hot air environment to the droplet is primarily through convection mechanism. The overall rate of evaporation and heat transfer depends on pressure and transport properties of the gas and the fuel. Depending on the droplet size, fuel properties and injector type, the injected droplets either get completely evaporated before reaching the combustor or it reaches the combustor in the form of smaller droplets dispersed in the air flow [2-4].

Droplet vaporization process has been modeled by several research groups particularly for a single droplet [5-13] and vaporizing turbulent sprays [14-16]. Maqua et al. [17] has reported experimental studies of the vaporization characteristics of monodisperse fuel droplets in airflow. They experimentally measured the droplet temperature using two-colour laser induced fluorescence thermometry. Similar experimental-work on monodisperse ethanol droplets injected into the thermal boundary layer of a vertical heated plate have been done by Castanet et al [18]. Maqua et al. [19] also reported a computational model of droplet evaporation comprising of two vaporizing species. However no researcher has studied the vaporization characteristics and flow dynamics of different biofuel blends.

In this work a numerical model has been developed to predict the vaporization characteristics of a biofuel droplet in a hot air stream along with a detailed experimental analysis and validation for

a levitated single droplet. Different types of fuels and fuel blends have been used to study the effect of droplet size and fuel type on the vaporization pattern. Furthermore, experiments involving IR-thermography of a convectively heated droplet in a levitator have been done to validate model development.

CHAPTER TWO: THEORY AND MODEL

In the current model, a single droplet has been considered. The effect of shape deformation due to aerodynamic force has been neglected. The heat transfer between the droplet and the air stream has been modeled by solving the energy equation. The diffusion and evaporation of different species within the droplet has been modeled by adopting the approach outlined by Sirignano [20]. There are three distinct parts in the model. The first part looks into instantaneous droplet velocity and displacement. The effect of the gravitation field has been neglected in this model. The air stream velocity is considered to be axial.

$$\frac{\partial U}{\partial t} = \frac{3C_D}{8r_s} \frac{\rho_\infty}{\rho_L} |U_\infty - U| (U_\infty - U) \quad (1)$$

$$\frac{\partial V}{\partial t} = -\frac{3C_D}{8r_s} \frac{\rho_\infty}{\rho_L} V^2 \quad (2)$$

$$\frac{\partial r_s}{\partial t} = -\frac{\dot{m}}{4\pi\rho_L r_s^2} \quad (3)$$

The drag coefficient C_D is defined by the correlation suggested in [21].

$$C_D = \frac{24}{\text{Re}(1 + B_{Mglobal})} \quad (4)$$

Reynolds number is defined as, $Re = \frac{2\rho_{\infty}r_s\sqrt{(U-U_{\infty})^2 + V^2}}{\mu_g}$. But the Spalding mass transfer

number, B_M is dependent on vaporization rate of different species. Also the properties like, viscosity μ_g depends on the average film temperature which is defined as $T_{film}=(2T_s+T_{\infty})/3$ [22].

The unknowns, film temperature and vaporization rates are calculated from the liquid phase analysis. Solution of the aforementioned Equations 1 to 3 will be used to compute the trajectory of the droplet and the diameter reduction within the air flow field.

The vapor phase solution surrounding the droplet is obtained considering a quasi-static analysis [20]. It can be justified by lower thermal diffusivity of liquid phase, which results in higher relaxation time. Clift et al. [23] suggested correlations for non-vaporizing spheres under this assumption.

$$Nu_o = 1 + (1 + Re.Pr)^{1/3} .f(Re) \quad (5)$$

$$Sh_o = 1 + (1 + Re.Sc)^{1/3} .f(Re) \quad (6)$$

The function $f(Re)$ in these equations is given by

$$\begin{aligned} f(Re) &= 1, Re \leq 1 \\ f(Re) &= Re^{0.077}, 1 \leq Re \leq 400 \end{aligned} \quad (7)$$

Due to surface blowing effect, the heat and mass transfer from the surface will be affected, which can be taken care of by introducing corrected Nusselt and Sherwood number [20].

$$Nu^* = 2 + \frac{Nu_o - 2}{F(B_T)} \quad (8)$$

$$Sh^* = 2 + \frac{Sh_o - 2}{F(B_{Mglobal})} \quad (9)$$

The effect of relative changes of film thicknesses is modeled as,

$$F = (1 + B)^{0.7} \frac{\ln(1 + B)}{B} \quad (10)$$

The Spalding heat and mass transfer coefficients are defined as [20],

$$B_T = \frac{C_{P,F}(T_\infty - T_s)}{h_{fg} + (Q_L / \dot{m})} \quad (11)$$

$$B_{M-global} = \frac{\chi_{v,\infty,i} - \sum_{i=1}^n \chi_{v,s,i}}{1 - \sum_{i=1}^n \chi_{v,s,i}} \quad (12)$$

where $\chi_{v,s,i}$, $\chi_{v,\infty,i}$ is mass fraction of 'i' th species at droplet surface and far field respectively. Here it is important to mention that in the current model both the species present in the droplet are volatile. A similar kind of numerical model with only one vaporizing species has been discussed in detail by Ozturk et al [24].

The total vaporizing mass flow rate can be calculated by the equation,

$$\dot{m} = 2\pi\rho_g D_{i\infty} r_s Sh^* \ln(1 + B_{M-global}) \quad (13)$$

The vaporization rate of individual species has been determined by using Raoult's Law [25]. The mass fraction for each vaporizing species is given by the relation [20],

$$\varepsilon_i = \chi_{v,s,i} - (\chi_{v,\infty,i} - \chi_{v,s,i}) / B_{M-global} \quad (14)$$

In the current work only two vaporizing species are considered and the rate of vaporized mass flux of each species can be expressed as

$$\begin{aligned} \dot{m}_1 &= \dot{m} \cdot \varepsilon_1 \\ \dot{m}_2 &= \dot{m} - \dot{m}_1 \end{aligned} \quad (15)$$

The velocity of the liquid at droplet surface can be calculated by equating the shear stresses across the droplet surface, which results in

$$U_s = \frac{1}{32} (U_\infty - U) \frac{\mu_g}{\mu_L} Re C_F \quad (16)$$

where, U_s is the liquid velocity at the surface, μ_g and μ_L are dynamic viscosity of liquid within the droplet and gas phase surrounding the droplet. The skin-friction factor C_F can be expressed by the correlation for Stefan flow given by [26]:

$$C_F = \frac{12.69 \text{Re}^{-2/3}}{1 + B_{M\text{-global}}} \quad (17)$$

The temperature and species concentration distributions in the liquid phase (inside the droplet) are given by the non-dimensionalized transient heat and mass convection-diffusion equations [20, 24].

$$\begin{aligned} \bar{r}_s^2 \frac{\partial \bar{T}}{\partial \tau} + \left(0.5 Pe_L \bar{V}_r \bar{r}_s - 0.5 \frac{dr_s}{d\tau} \eta \right) \frac{\partial \bar{T}}{\partial \eta} + 0.5 Pe_L \frac{\bar{V}_\theta \bar{r}_s}{\eta} \frac{\partial \bar{T}}{\partial \theta} = \\ \frac{1}{\eta^2} \frac{\partial}{\partial \eta} \left(\eta^2 \frac{\partial \bar{T}}{\partial \eta} \right) + \frac{1}{\eta^2 \sin \theta} \frac{\partial}{\partial \theta} \left(\sin \theta \frac{\partial \bar{T}}{\partial \theta} \right) \end{aligned} \quad (18)$$

$$\begin{aligned} Le_L \bar{r}_s^2 \frac{\partial \bar{\chi}_i}{\partial \tau} + \left(0.5 Pe_L Le_L \bar{V}_r \bar{r}_s - 0.5 Le_L \frac{dr_s}{d\tau} \eta \right) \frac{\partial \bar{\chi}_i}{\partial \eta} + 0.5 Pe_L Le_L \frac{\bar{V}_\theta \bar{r}_s}{\eta} \frac{\partial \bar{\chi}_i}{\partial \theta} = \\ \frac{1}{\eta^2} \frac{\partial}{\partial \eta} \left(\eta^2 \frac{\partial \bar{\chi}_i}{\partial \eta} \right) + \frac{1}{\eta^2 \sin \theta} \frac{\partial}{\partial \theta} \left(\sin \theta \frac{\partial \bar{\chi}_i}{\partial \theta} \right) \end{aligned} \quad (19)$$

The dimensionless quantities employed here are $\bar{r}_s = r/r_o$, $\tau = \alpha_L t/r_o^2$, $\eta = r/r_s$, $\bar{T} = (T - T_o)/T_o$, and $\bar{\chi}_i = (\chi_i - \chi_{i,o})/\chi_{i,o}$ where r_o is the initial radius, α_L is thermal diffusivity of the liquid, t is

time, r_s is the radius of droplet surface, T is temperature with T_o being the initial value and correspondingly χ_i being the mass fraction of 'i'th species with $\chi_{i,o}$ being its initial value. $Pe_L = (r_s \Delta U) / \alpha_L$ is the liquid Peclet number and $Le_L = D_s / \alpha_L$ is the liquid Lewis number. \bar{V}_r and \bar{V}_θ are the radial and angular components of the velocity within the droplet which can be calculated by considering the Hill's spherical vortex assumption [27],

$$V_r = -U_s \left(1 - \frac{r^2}{r_s^2}\right) \cos \theta \quad \text{and} \quad V_\theta = U_s \left(1 - 2 \frac{r^2}{r_s^2}\right) \sin \theta \quad (20)$$

The boundary conditions for Equations 18 and 19 can be written as,

$$\left. \begin{matrix} \bar{T} \\ \bar{\chi}_i \end{matrix} \right\} (\tau=0) = 0 \quad \text{and} \quad \left. \frac{\partial}{\partial \eta} \begin{matrix} \bar{T} \\ \bar{\chi}_i \end{matrix} \right\} \Big|_{\eta=0} = 0 \quad \text{and} \quad \left. \frac{\partial}{\partial \theta} \begin{matrix} \bar{T} \\ \bar{\chi}_i \end{matrix} \right\} \Big|_{\theta=0,\pi} = 0 \quad \text{and}$$

$$\left. \frac{\partial}{\partial \eta} \begin{matrix} \bar{T} \\ \bar{\chi}_i \end{matrix} \right\} \Big|_{\eta=1} = \begin{cases} \int_0^\pi \frac{\partial \bar{T}}{\partial \eta} \sin \theta d\theta = \frac{Q_L}{2\pi r_s k_L T_o} \\ \int_0^\pi \frac{\partial \bar{\chi}_i}{\partial \eta} \sin \theta d\theta = \frac{\dot{m} \bar{\chi}_i - \dot{m}_i}{2\pi r_s \rho_L D_{i,s} \chi_{z,o}} \end{cases} \quad (21)$$

where Q_L is the total heat flux to the droplet, k_L is the conductivity of the liquid, ρ_L is liquid density inside the droplet, $D_{i,s}$ is the mass diffusivity of solute in solvent. Further details of this model can be found in [19, 20, 24].

Equations (1-15) along with the governing partial differential equations for conservation of energy and species concentration (18-19) in the liquid phase (inside the droplet) can be solved

iteratively to obtain the species concentration and temperature distribution within the vaporizing droplet. The above equations have been solved using modified Dufort-Frankel technique.

CHAPTER THREE: EXPERIMENTAL SET UP

To validate the model proposed in this work, an experiment has also been designed to study vaporization characteristics of selected biofuel blends. An ultrasonic levitator (Tec5 ultrasonic levitator, 100 kHz) and an IR camera have been used for levitation and thermal imaging of biofuel droplets as shown in Figure 1.

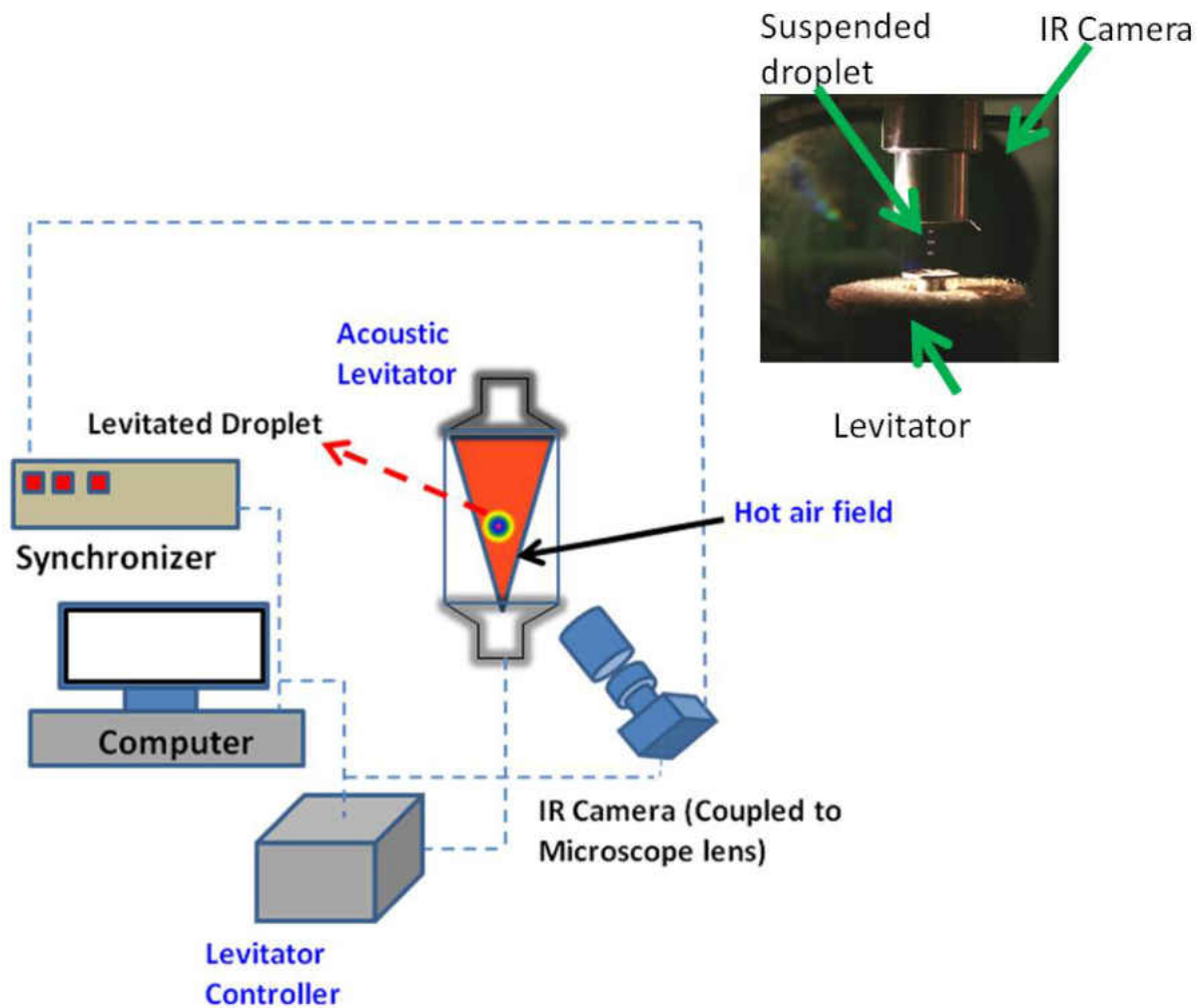


Figure 1: Experimental setup

The droplets are generated and deployed into the pressure nodes of levitator using a micro needle. After the droplet is suspended successfully, a moderately heated (35°C) air flow is supplied coaxially around the droplet. The velocity of the air field was maintained around 2.0 m/s. The vaporization pattern of the droplet was captured with an IR Camera (FLIR Silver: calibrated for a range of -5 to 200°C with an accuracy of +/- 1°C). The IR camera was attached to a microscopic zoom lens (FLIR G3-F/2) which is specially made for transmitting mid-range IR wavelengths. This lens has a 3x magnification with a working distance of around 40mm. The associated software 'ALTAIR' has been used for capturing and processing the images. Both the camera and levitator sat on X-Y stages which allowed micrometer adjustment to accurately focus the camera on the droplet.

IR-thermography or temperature measurement through IR camera is based on radiation. The IR camera captures the infrared emission from a surface and it is pre calibrated to convert the intensity of the irradiation at each pixel of the imaging plane into a temperature scale. The FLIR camera used for current experiment is pre-calibrated to measure a temperature range -5 to 200°C. However, the upper and lower limit of the temperature scale is dependent on the integration time used for a particular experiment. Lower temperature ranges require higher integration time, which in turn reduces the maximum imaging rate (frames per second) of the camera. During the current experiment, an optimum integration time of 1.6 msec has been used, using which a temperature range of 15-55°C could be measured. The pre-calibration of the camera has been performed for an object with emissivity of 1. However, the image processing software can be used to modify the emissivity to obtain corrected temperature.

The camera was operated at a rate of 50 frames per second and was triggered by a two channel delay generator. The low air temperature and velocity around the droplet resulted in long heating time. This allowed the use of the IR camera to measure the droplet surface temperature and size simultaneously at a given time instant. Three sets of recording have been performed for each condition to ensure repeatability of the experiment. The initial drop size was repeatable within 2.5%. There were minor oscillations in the droplet location which made the droplets go in and out of the focus plane. These out of focus images were not considered for data analysis.

To extract the average temperature and diameter at any time instant, a linear line of interest has been defined along the diameter of the droplet. For each image, this line (zone of interest) was defined in such a way that it corresponds to the projection of the droplet surface on the diameter of the droplet. The mean temperature along that line is taken as representative temperature of droplet surface at that time instant.

CHAPTER FOUR: RESULTS AND DISCUSSIONS

Different types of fuels and their blends investigated for this computation modeling are tabulated in Tables 1 and 2. In reality, fuels like RME and diesel are comprised of many molecular species. However to avoid numerical complexity, RME, gasoline and diesel are considered to be single component surrogate fuels with transport properties representative of the bulk (averaged) behavior of the real multicomponent fuel. The properties of pure fuels are tabulated in Table 3. In the case of mixed blend fuels, the bulk properties of the mixture such as density, thermal conductivity, viscosity are calculated based on mixture laws. The vapor pressures for all four major fuels studied in current work are shown in Figure 2. It can be seen that vapor pressure is a monotonically increasing function of temperature for all the fuels. Vapor pressures of gasoline and ethanol are higher than those of diesel and RME. At lower temperature (below 550 K), vapor pressure of RME is lower than vapor pressure of diesel, but at temperatures above 550 K, the RME vapor pressure is higher than that of diesel.

Table 1: RME-Diesel blends

Fuel blends of RME-Diesel	Mass fraction of RME	Mass fraction of Diesel
Pure Diesel	0%	100%
RME-Diesel 10-90%	10%	90%
RME-Diesel 20-80%	20%	80%
RME-Diesel 50-50%	50%	50%
Pure RME	100%	0%

Table 2: Ethanol-Gasoline blends

Fuel blends of Ethanol-Gasoline	Mass fraction of Ethanol	Mass fraction of Gasoline
Pure Gasoline	0%	100%
Ethanol-Gasoline 10-90%	10%	90%
Ethanol-Gasoline (20-80%)	20%	80%
Ethanol-Gasoline (50-50%)	50%	50%
Pure Ethanol	100%	0%

Table 3: properties of pure fuel

	Diesel	Ethanol	Gasoline	RME
Density (kg/m ³)	846	790	790	880
Specific Heat (J/kg-K)	2300	2550	2550	2300
Thermal Conductivity (W/m-K)	0.182	0.17–2.29e- 4 * (T(K)- 250)	0.17– (0.16/700) * (T(K)-250)	0.182
Latent heat (J/Kg)	254000	904000	317700	254000
Vapor Pressure (kPa) $P * 10^{\{A+B/(T(K)+C)\}}$ A,B,C, D are constants	A= 0.21021 B=- 440.61 C=- 156.896 P=100	A=8.04494 B=-1554.3 C=-50.5 P= 0.1333	A= 4.02832 B= -1268.636 C= - 56.199 P= 100	*
Dynamic viscosity (Pa-s)	0.00389	0.00037	0.00037	0.00389

(Properties are taken from ref [[16], [26)], T(K) = Temperature in K ; *: mass average vapor pressure of all the esters present in RME

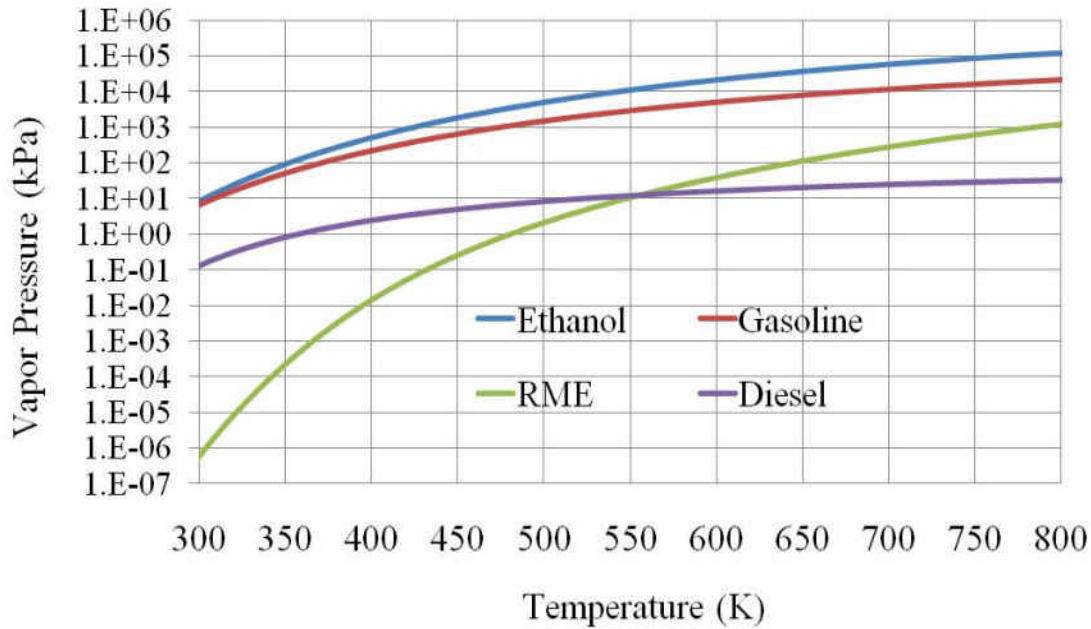


Figure 2: Vapor pressures of different fuels

Validation of Numerical results with Experiments

For the validation experiment, a droplet was suspended in an air flow of 2.0 m/sec at a temperature of 308 K. Water droplet with an initial diameter of 800 μm was used only to validate the relative trend. Change in droplet diameter and temperature with time were captured by IR thermography as described in previous section. In addition to the water droplet, three blends of ethanol-gasoline droplets were used.

To extract the temperature and diameter, a linear zone of interest is defined along the diameter of the droplet, as given in the inset of Figure 3. It can be noted that there is a variation in temperature along that line. Correction for emissivity has also been done for that linear zone of

interest. Emissivity for water has been reported between 0.95-0.98 [29, 30]. The change in temperature due to change in emissivity was 0.03°C which was assumed to be negligible.

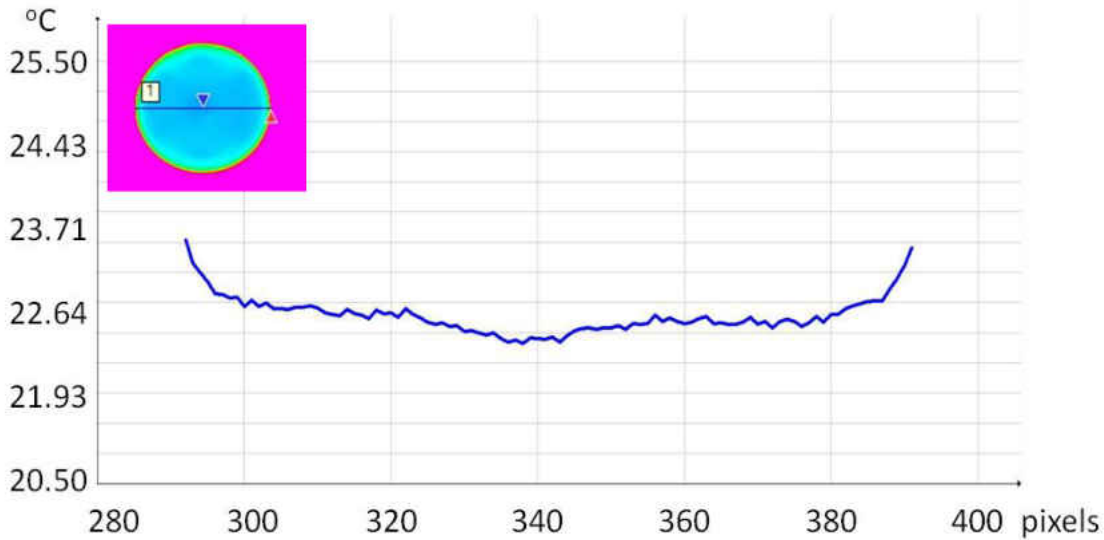
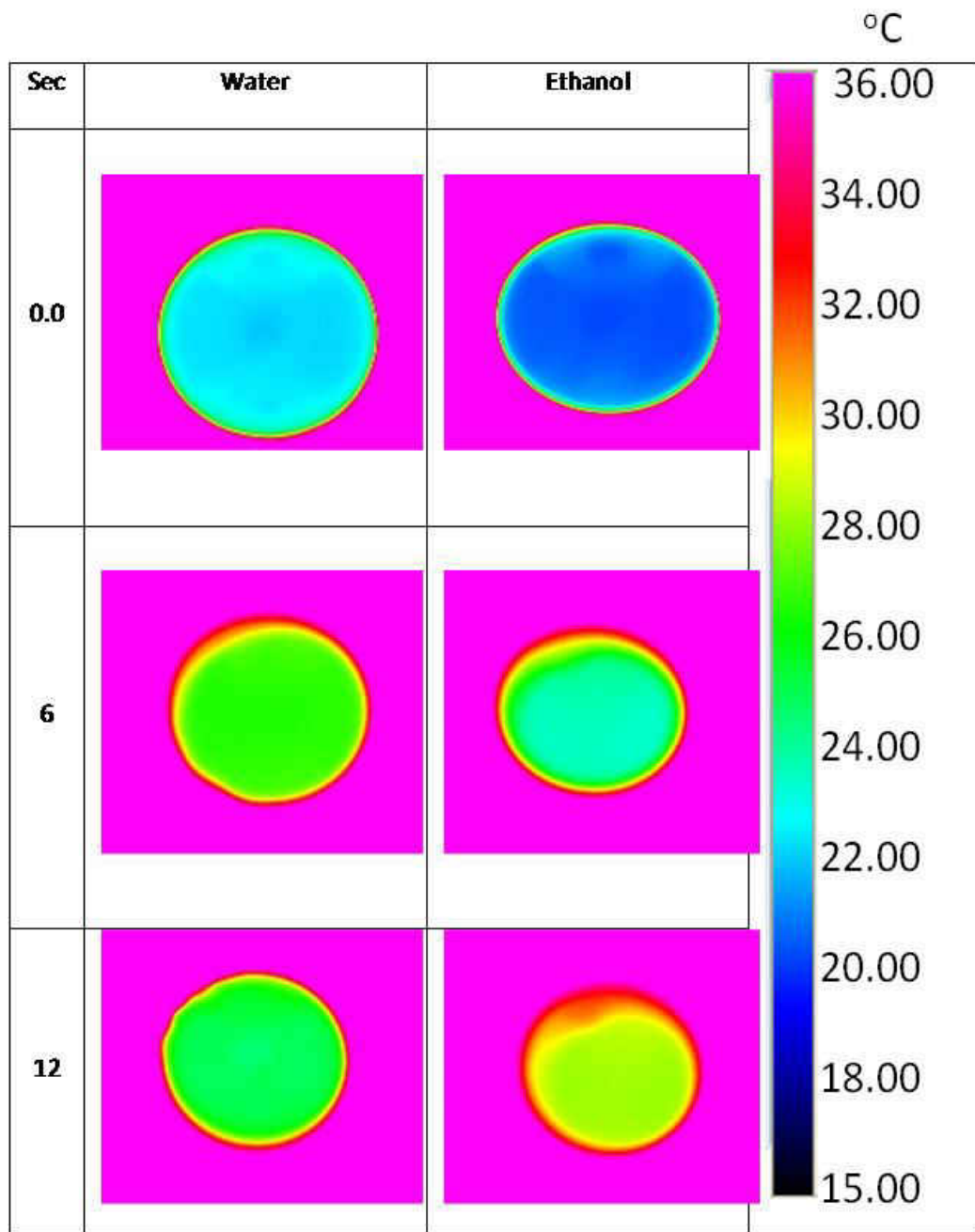
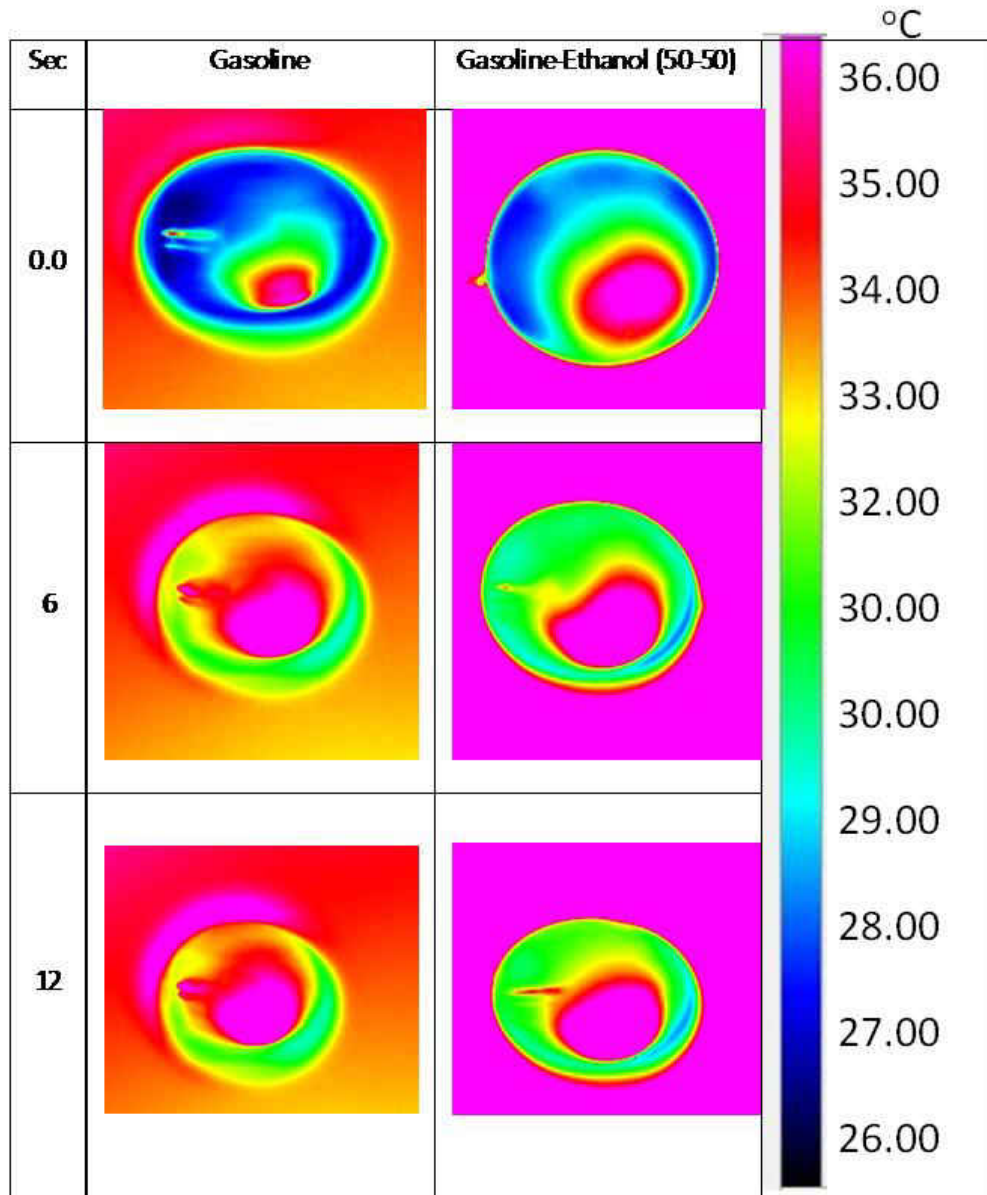


Figure 3: Sample image processing: Temperature distribution along the linear zone of interest. Inset: Sampled zone of interest in a water droplet after 1 sec of heating.

Figure 4 shows IR images for water, ethanol, gasoline and gasoline-ethanol blend. From these images, both temperature and droplet size can be obtained. The temperature and velocity of the flow field around the droplet are small and the droplet diameter is large, hence the vaporization rate is very slow. The droplet in some cases showed deformation in shape due to the acoustic field of the levitator. This phenomenon has been also reported by Yarin et al [31]. Temperature measurements for gasoline and ethanol-gasoline blends were not possible, due to the fact that gasoline has high IR transmissibility, which leads to errors in IR thermography. However, high transmissibility does not contaminate the analysis for determining the droplet size at each time instant.

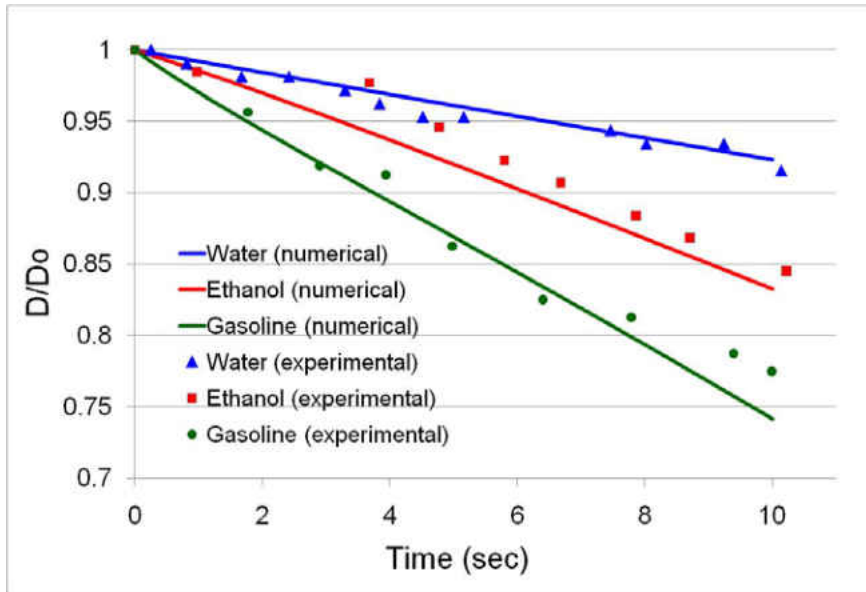


a)

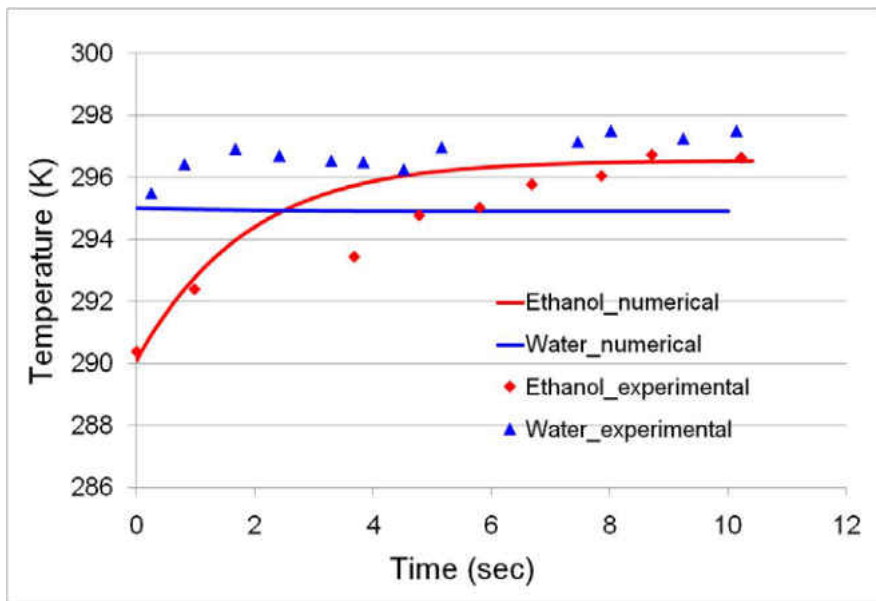


b)

Figure 4: IR images showing droplet size reduction and surface temperature variation for four different fuel blends at different time instants. a) water and ethanol, b) gasoline and gasoline-ethanol (50-50)



a)



b)

Figure 5: 800 μm droplets of different species; a) diameter reduction (D_0 is initial diameter, 800 μm) b) droplet surface temp evolution (D_0 is initial diameter, 800 μm).

Yarin et al. [31] presented a detailed numerical analysis of vaporization process of a droplet suspended in an ultrasonic levitator. Their work highlighted the fact that presence of strong acoustic field and surface blowing effect in acoustic levitator strongly dominates the vaporization characteristics over natural mass diffusion. However, they also explained that if the acoustic field is weak and the droplet is small compared to pressure wavelength, then the acoustic field does not have much effect on the droplet vaporization. Similar findings are also reported by Seaver [32] and Tian [33]. In the current experimental set up, a weak 154 dB sound wave of frequency of 100 kHz has been used, which confirms that droplet size is very small compared to pressure wavelength. Thus acoustic field would not have much effect on vaporization allowing the numerical model described in section 2. Figure 5a shows the comparison of diameter variations observed in the experiment with the numerical results. Figure 5b compares the surface temperatures obtained by experiment and numerical model for different blended fuels. The diameter and temperature plots in Figures 5a and 5b show that the comparison between the experimental and numerical results is reasonable. The variation of surface temperature from IR images is about 1°C as seen in Figure 3. The numerical methodology assumes that at any given time instant the droplet surface temperature is constant [11]. The boundary condition for temperature at outer radius is given in Equation 21. It determines the slope of the temperature by calculating total heat transfer from the droplet surface. The heat transfer around the droplet is assumed to be same, that leads to equal surface temperature assumption. This results in some discrepancy between the experimental and numerical results. In addition, the model assumes the droplet to be azimuthally symmetric, which in reality is not true. The water, ethanol and gasoline used for the experiment are commercially available grade. They may contain some impurities

which could change the properties (like latent heat, specific heat, density and thermal conductivity) to some extent.

Validation for the case of bi-component blends

To verify the validity of the proposed model, a case of acetone-ethanol (50%-50%) blend has been studied and the obtained results are compared with the results reported by Maqua et al, [19]. For the case of a droplet of 130 μm initial diameter, the temperature and contour plots are shown in Figure 6, 6.5 msec after injection. It can be observed that droplet diameters are around 120 μm in both cases. The mass concentration distribution predicted by Maqua et al [19] is very similar to the results predicted by the current model. However, there is a mismatch in droplet temperature. Maqua et al reported average droplet temperature to be around 25°C, while in current work, it was found to be around 40°C. This discrepancy can be due to their assumption of a decaying temperature profile for the flow field, while in current work a uniform temperature field has been used. Maqua et al. [19] reported only the center line temperature and velocity profiles of the air stream. However, for current numerical simulation, overall temperature and velocity profiles of the entire air field is required. Hence a uniform temperature field was used for global comparison in the current work.

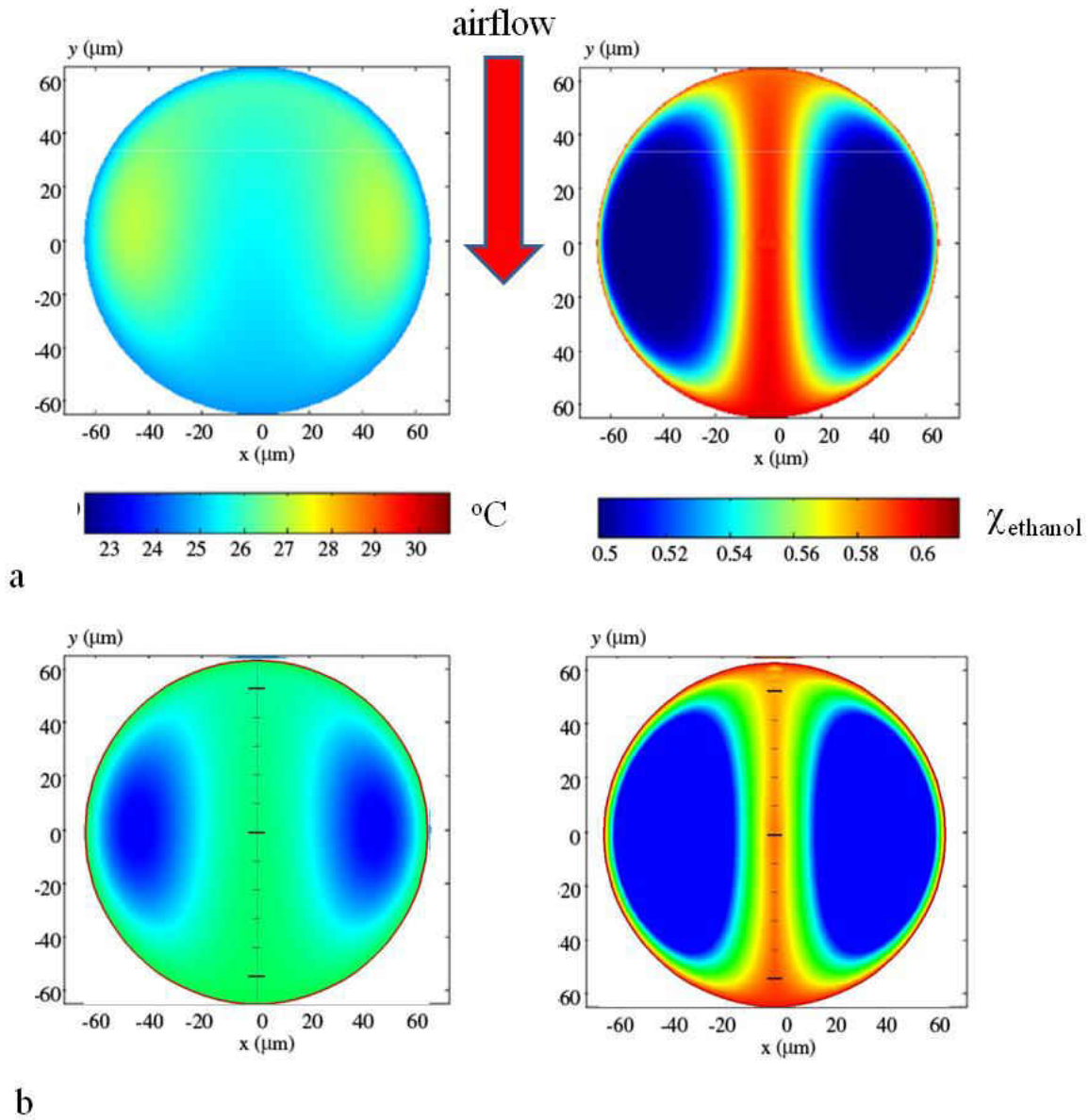


Figure 6: Temperature and Ethanol mass fraction profiles in a droplet 6.5 msec after the start of the heating process; a) Maqua et al [19] b) Current work. Initial diameter is 130 μm .

Computational Results in the Premixer

The computational domain represents a typical pre-mixer with a length of 30 cm and height of 5 cm. Air is introduced into the chamber at a constant velocity and temperature of 10 m/sec and 800 K respectively. The fuel droplets in the pre-mixer are injected transversely with a vertically downward velocity of 1 m/sec. The injector is located at the top surface of the pre-mixer chamber at a distance of 3 cm downstream of the air inlet.

a) Comparative studies of blended fuels:

The droplet starts vaporizing after being injected into the hot air environment in the levitator, which causes a reduction in diameter. The vaporization rate depends on fuel properties like vapor pressure, latent heat and specific heat at constant pressure of vapor phase. So, the droplets containing different blended fuels will have different vaporization patterns. The vaporization rate is dependent on the droplet size as well. In the actual premixer, generally the injected droplets exhibit a wide range of diameters. In this work, investigations are done for two distinct droplet sizes of a) 400 μm and b) 20 μm .

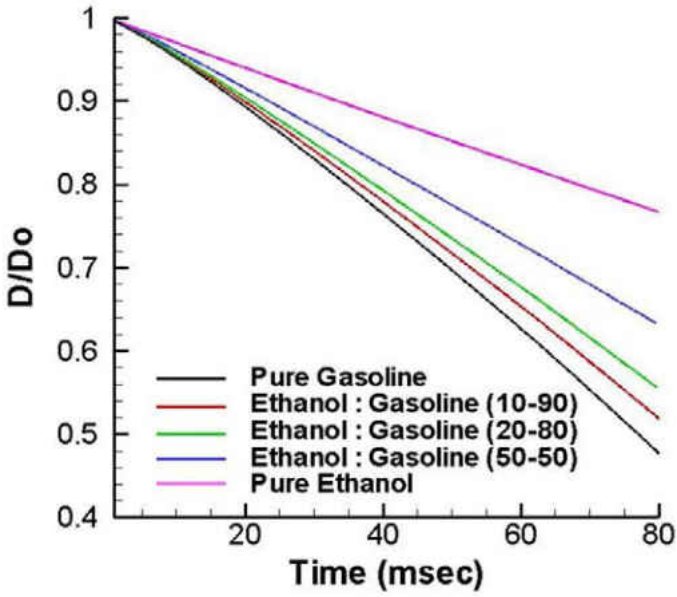
The next section presents a comparative analysis of different blends by analyzing diameter reduction, surface temperature, and concentration evolution within the droplet. In this work, the concentration considered for all cases are denoted in terms of mass fractions.

i) Ethanol-gasoline blends:

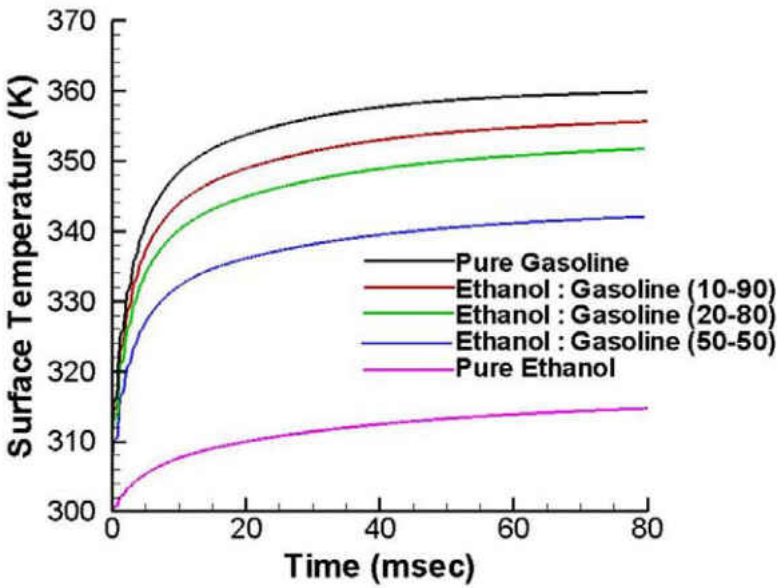
400 μm droplet

For the initial droplet size of 400 μm , Figure 7 shows that pure gasoline droplet vaporizes faster than pure ethanol. Also it shows that for ethanol-gasoline blends, increase in gasoline percentage

causes faster vaporization rates. This appears to be counterintuitive at first as the vapor pressure of ethanol is higher than that of gasoline at the same temperature (see Figure 2) and the vaporization rate is faster for higher vapor pressures, according to equation 13. But this can be explained from the surface temperature plots of the different ethanol-gasoline blended droplets in Figure 7b. For pure ethanol droplets, the temperature reaches around 315K, while the surface temperature of pure gasoline droplets reaches as high as 360K. The blends attain intermediate temperatures between these two limits depending on relative percentages of gasoline and ethanol. This is because the latent heat of vaporization for ethanol (904 kJ/kg) is almost three times higher than that of gasoline (317.7 kJ/kg). In other words ethanol droplets will need almost three times higher sensible heat for the same temperature rise compared to the gasoline droplet. Thus, the effect of latent heat is reflected in the surface temperature plot, as the surface temperature of the droplet determines the corresponding vapor pressure. Figure 7b also shows that temperature rise for gasoline droplet is faster than ethanol droplet.. From Table 2, comparing vapor pressure at these temperatures shows that ethanol vapor pressure (20 kPa @ 315 K) is significantly lower than that for gasoline (70 kPa @ 360 K). The vaporizing characteristics of pure droplets behave as two extreme cases for blended droplets.



a)



b)

Figure 7: 400 μm droplets of different fuel blends a) diameter reduction (D_0 is initial diameter, 400 μm) and b) surface temperature (in K) variation

Due to differences in latent heats, the temperature rise would be faster in gasoline compared to ethanol. However, due to thermal diffusion the surface temperature of the droplet will achieve an intermediate value depending on the mass fraction of the two species. Higher mass fraction of gasoline will result in higher surface temperature. This trend can be observed in Figure 7b. That justifies the fact that fuel blends with higher gasoline mass fraction will have higher vapor pressure resulting in faster vaporization rate, and therefore will have higher diameter reduction. However, the vapor pressure of ethanol is higher than that of gasoline at any given temperature in a blend. So at the surface, where both ethanol and gasoline are at same temperature, ethanol portion will vaporize faster than gasoline for any given blend of ethanol gasoline droplet. In other words concentration of ethanol at the droplet surface will always decrease. Figure 8 shows that surface concentration of ethanol indeed decreases with time in different ethanol gasoline blends.

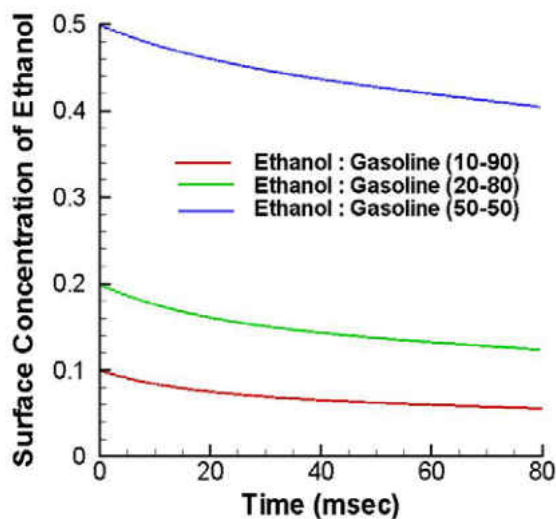
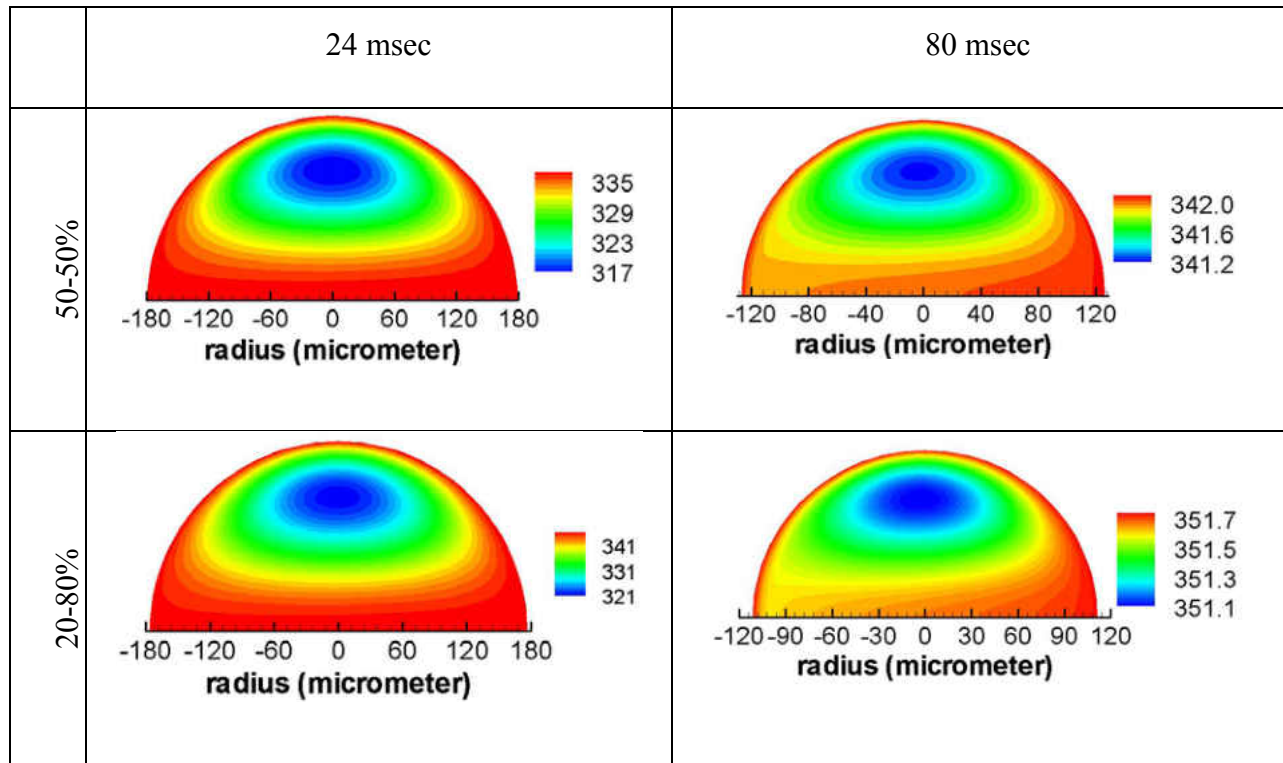
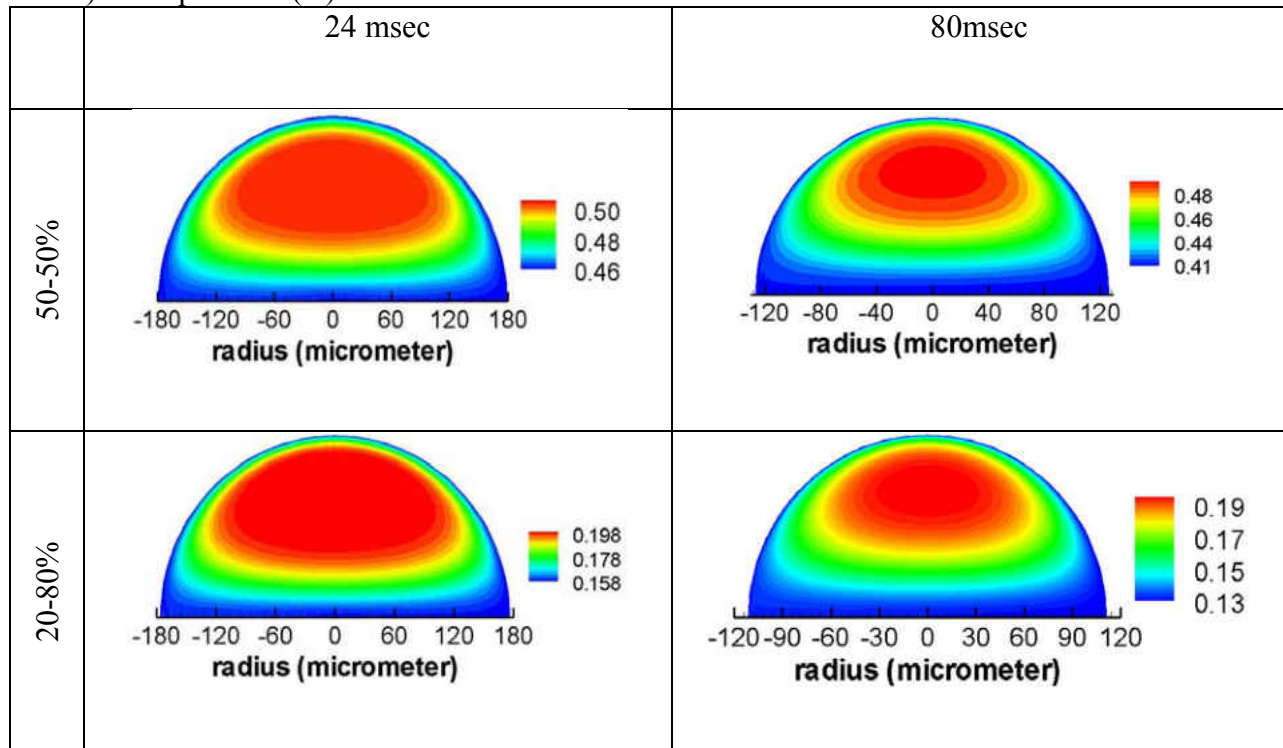


Figure 8: Surface concentration (mass fraction) variation with time for 400 μm droplet; Ethanol-Gasoline blends



a) Temperature (K)



b) Concentration (mass fraction of ethanol)

Figure 9: a) Temperature b) Ethanol concentration distributions at two time instants for ethanol-gasoline blended droplets (initial diameter 400 μm).

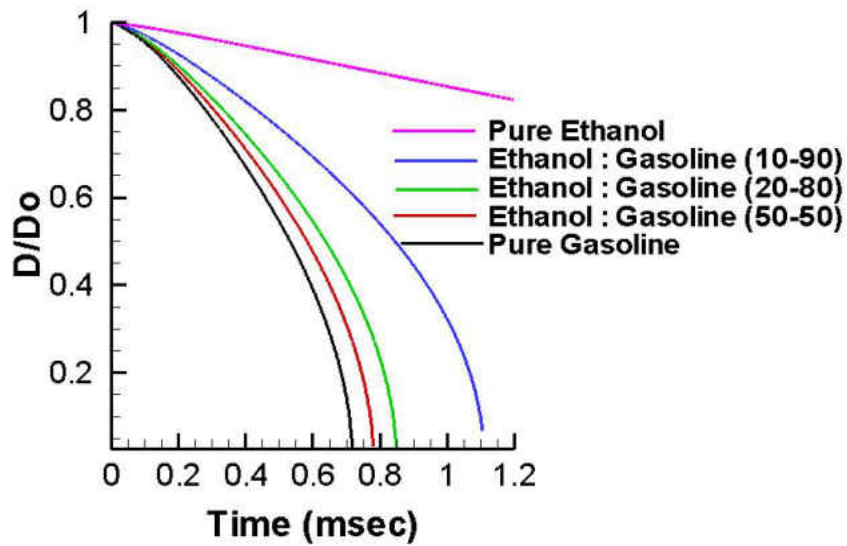
Figure 9 shows the temperature and ethanol concentration distributions within an ethanol-gasoline 50-50 and 20-80 droplet at different time instants. It can be noted in Figure 9a, that during initial time instants, there is a sharp temperature gradient present within the droplet. However, with time this gradient diminishes. Depending on the values of thermal diffusivity, the rate of temperature equilibration inside the droplet can be different for different fuel types. It can be observed in Figure 9b, that the local concentration of ethanol is constant along the surface and horizontal diameter. This zone behaves like an isoconcentration zone which engulfs higher concentration zone inside it. This kind of distribution provides evidence of strong recirculation within the droplet. Higher Peclet number of the species is responsible for strong convective circulation within the droplet.

As noted earlier, the surface concentration of ethanol decreases with time for blended fuel droplets. This also implies that ethanol concentration will be higher towards the center compared to the surface. So ethanol near the center of the droplet will diffuse towards the surface, which eventually lowers the concentration near the center. This pattern can be observed in Figure 9b, where it shows that initially the concentration near the center is 0.5, which reduces to 0.48 at longer time instants. Figure 9 also represents temperature and concentration contours for 20-80 blend of ethanol-gasoline droplets for two different time instants. For the two blends shown (and all the blends not shown), there exists a sharp temperature gradient initially within the droplet which diminishes with time. On the other hand, the concentration distribution shows more or less

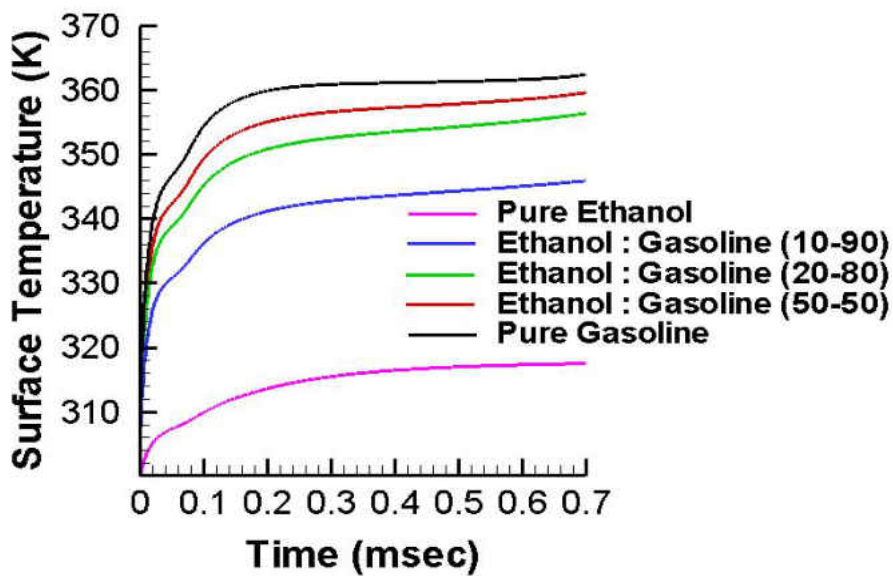
the same gradient throughout the vaporization lifetime. This is due to the fact that thermal diffusivity is much higher compared to mass diffusivity. In other words, thermal diffusion is a faster mechanism bringing the droplet to quicker temperature equilibrium than mass diffusion equilibrium. The iso-concentration lines shown in Figure 9b depict the presence of strong recirculation with very low diffusion resulting from low mass diffusivity of ethanol in gasoline.

20 μm droplet

For gasoline-ethanol blends of fuel, the smaller droplets (20 μm diameter) exhibit similar characteristics like the larger droplets (400 μm) as shown in Figure 10. The time scale of vaporization is lower for smaller droplets due to their lower mass. The droplet nearly completely vaporizes for all blends leading up to 100% gasoline within 1.1ms. For these smaller droplets internal circulation is less effective, resulting in less mixing of hot fluid at the surface and colder fluid near core of the droplet. This increases surface vaporization of the droplet. As seen for large droplets, the vaporization rate for pure ethanol is lower than pure gasoline and its blends. Again, it is due to the fact that higher latent heat of ethanol is responsible for its slower temperature rise compared to gasoline. The vapor pressure being a monotonically increasing function of temperature, the vaporization rate also increases with temperature, and hence for blended fuels, vaporization rate becomes faster with increase in gasoline mass fraction.



a)



b)

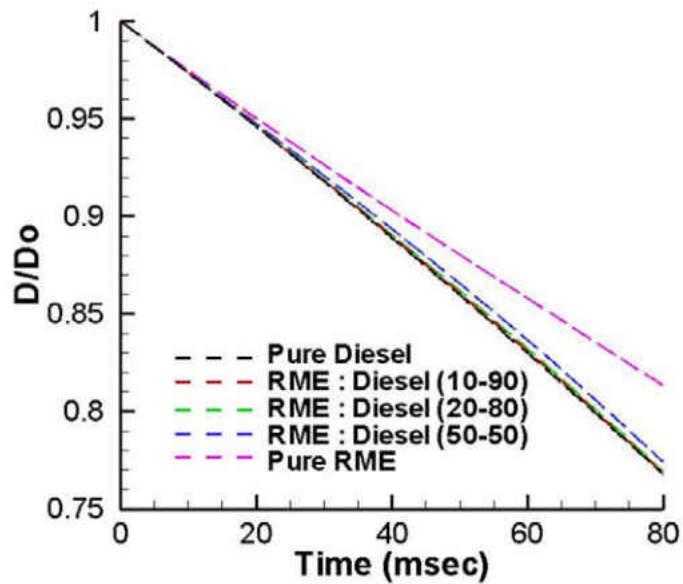
Figure 10: 20 μm droplets of different fuel blends a) diameter (D_0 is initial diameter, 20 μm) reduction and b) surface temperature (in K) variation

ii) RME Diesel Blends

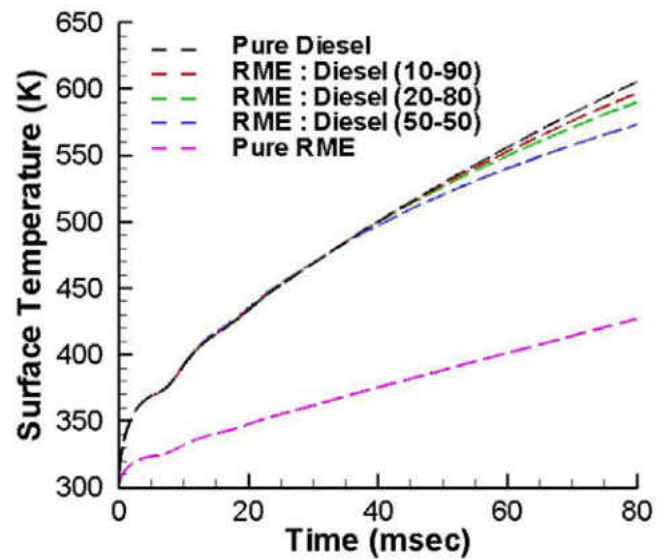
Esters derived from different fatty acids are a kind of biofuel which is heavy and less volatile than alcohol based fuels. Rapeseed Methyl Esters (RME) is a culmination of different fatty acids esters. The properties of RME being very similar to diesel, it is considered to be a substitute fuel for diesel. As mentioned in Table 1b, in this section different RME-diesel blends are studied.

400 μm droplet

Figure 11 shows that pure diesel droplet vaporizes faster than pure RME droplets. The rate of temperature rise is faster in case of pure diesel droplets as shown in Figure 11b. Figure 2 shows that for temperatures less than 550 K, vapor pressure of diesel is higher than that of RME. Initially at low temperatures (for both pure diesel and RME droplets), vapor pressure is much higher for diesel. That makes the diesel droplets vaporize faster than RME. This is shown in Figure 11a. However, as described earlier, for blended biofuels depending on the relative mass fractions of two species, the surface temperature attains intermediate values between pure diesel and pure RME. The RME vapor pressure shows a sharp gradient with temperature. As the blended fuels exhibit higher surface temperature than that of pure RME droplets (Figure 11a), the vaporization rate increases (faster diameter reduction).



a)



b)

Figure 11: 400 μm droplets of different RME-diesel fuel blends a) diameter (D_0 is initial diameter, 400 μm) reduction and b) surface temperature (in K) variation

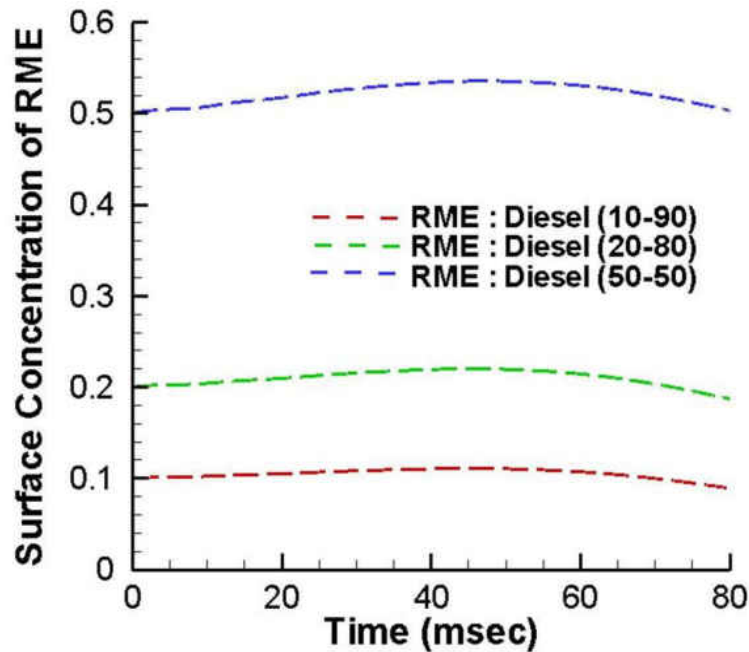
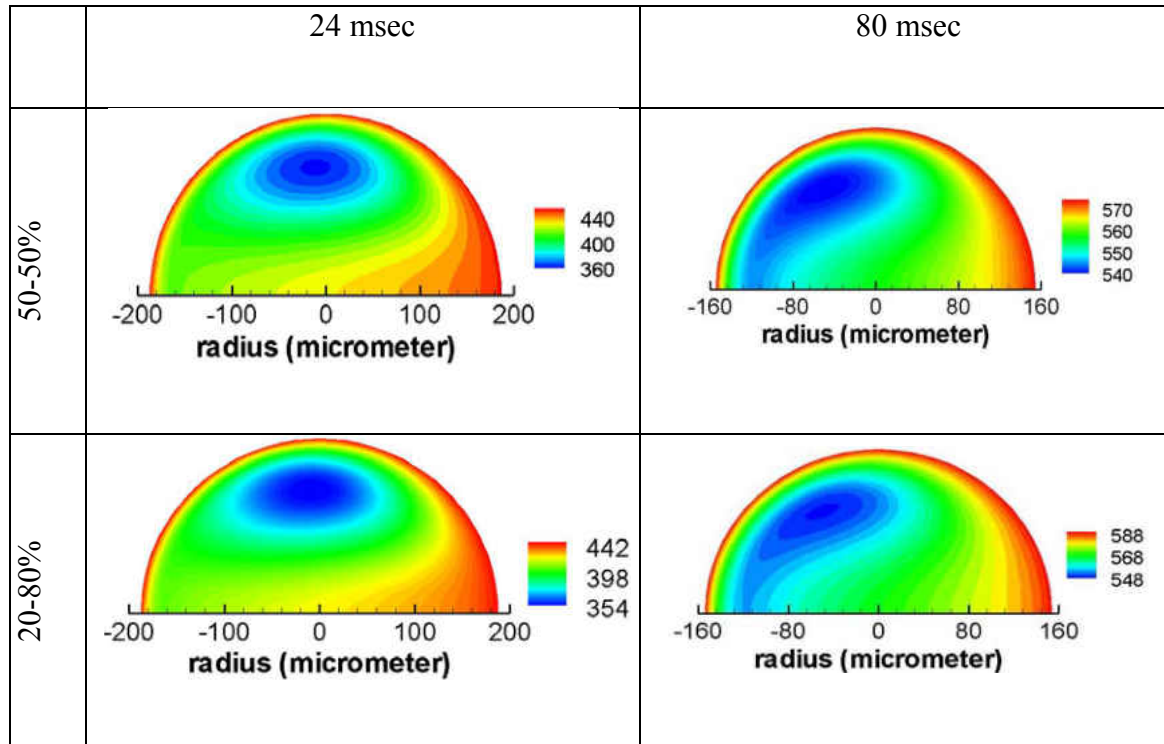


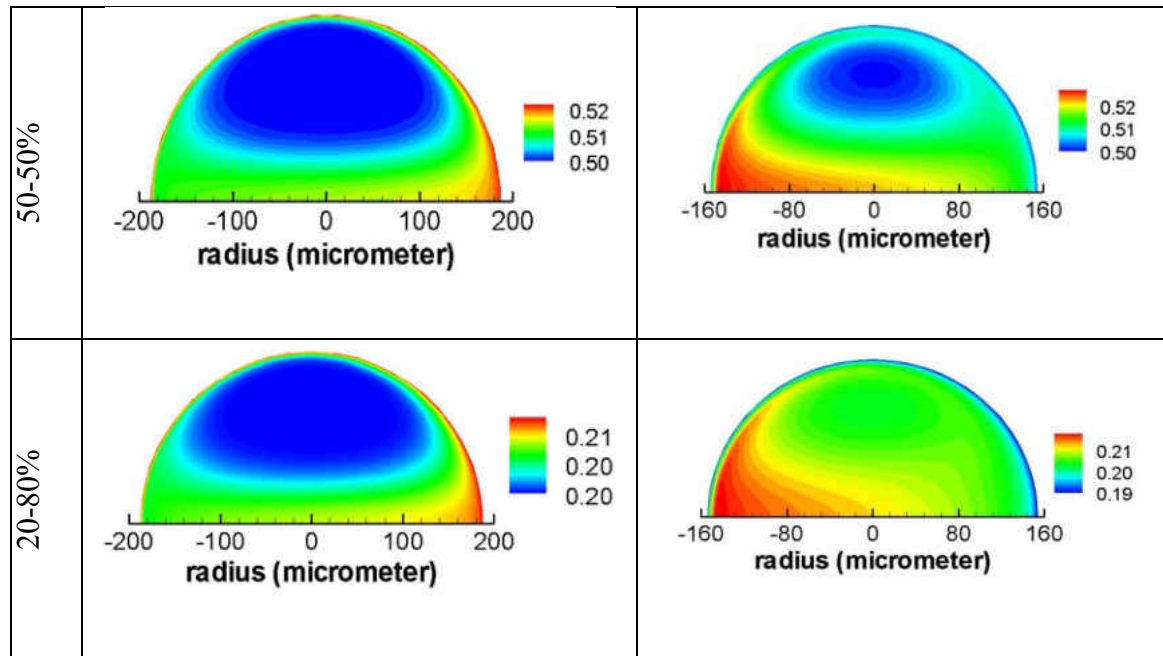
Figure 12: Surface concentration (mass fraction) variation with time for 400 μm droplets (RME-Diesel blends).

As shown in Figure 11, at $\sim 60\text{ms}$, the surface temperature of RME and RME-diesel blends reaches 550K. Until the surface reaches 550K, vapor pressure of diesel is higher than RME. Therefore, as seen in Figure 12, there is an increase of concentration up to about 550K. Beyond this temperature, the vapor pressure of RME becomes higher than diesel causing vaporization of RME to increase and concentration to fall. The exact intersecting point of vapor pressures for RME and diesel is around 550 K. However, it is observed that the inflection point for surface concentration profile of RME occurs at a temperature of around 530 K. This can be attributed to the fact that during initial slower vaporization rate, there is a concentration build up of RME compared to diesel. It can also be noted that the vapor pressure of these two species become comparable when the surface temperature reaches a value around 525 K. As the surface has

higher concentration of RME than diesel and the vapor pressures are almost similar, the cumulative vaporization rate of RME becomes higher than that of diesel around a temperature of 530 K.



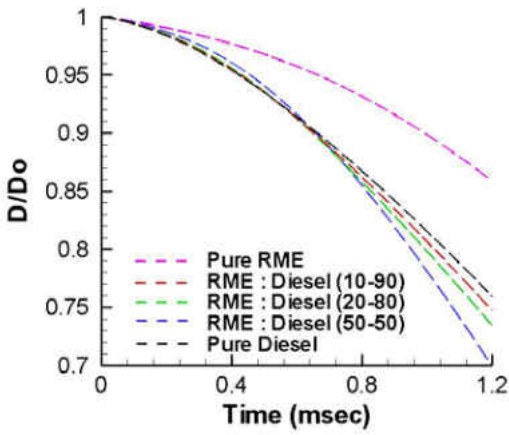
a) Temperature (K)



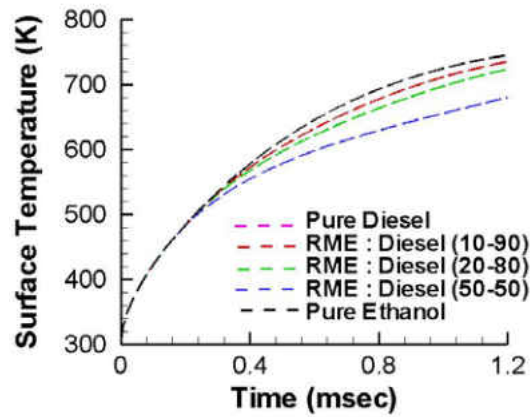
b) Concentration

Figure 13: a) Temperature b) RME concentration distributions at two time instants for RME-Diesel droplets (initial diameter 400 μm).

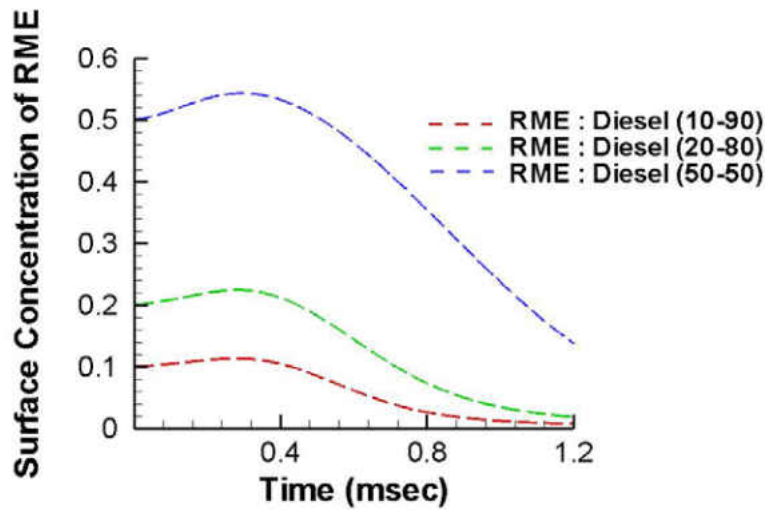
Figure 13 depicts the temperature and RME concentration distribution within different RME-Diesel blended droplets. Figure 13a shows the presence of sharp temperature gradient within the droplets along with the recirculation patterns within the droplets. Figure 13b shows the RME concentration contours within blended droplets. Initially, the faster vaporization of diesel leads to an increase in RME concentration at the droplet surface while the core of the droplet remains almost at the initial value. However, as the RME vaporization rate becomes faster than diesel towards the later part of the vaporization process, the surface concentration of RME decreases and becomes lower than the concentration near the core.



a)



b)



c)

Figure 14: 20 μm droplets of different RME-diesel fuel blends a) diameter (D_0 is initial diameter, 20 μm) reduction, b) surface temperature (in K) variation and c) Surface concentration (mass fraction of RME)

20 μm droplet

For smaller fuel droplets, there are some noticeable changes in the vaporization pattern. Figure 14 shows that pure diesel droplet vaporizes faster than pure RME droplet, which was also observed in the case of 400 μm droplet. The pure diesel droplet attains a surface temperature of 750K, while pure RME droplet reaches a temperature of only 550K. Comparison of vapor pressure for these two species at corresponding temperature reveals that for diesel droplets vapor pressure is around 30 kPa, while that for RME is around 10 kPa. Thus vaporization of pure diesel droplet is faster than pure RME, which is reflected in Figure 14a.

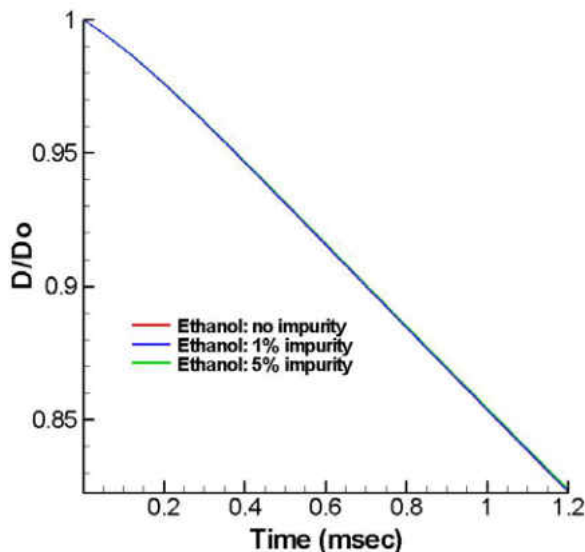
However, unlike the 400 μm case, for 20 μm droplets blended fuels showed a faster vaporization rate than pure diesel droplet. As discussed earlier, for blended bio fuels depending on the relative percentage of two species, the droplet will attain some temperature between two extreme cases marked by pure RME and pure Diesel. Figure 14b shows that the surface temperature of blended fuels reaches \sim 650-720K. Referring to the vapor pressure values of RME and diesel, it reveals that at temperature range of 650K, vapor pressure of RME becomes as high as 110kPa. It increases further with temperature. It is understandable that in blended fuels, the RME portion will vaporize faster and thus the blended fuels will show faster vaporization than pure diesel.

It can also be noticed that (Figure 14a), at lower time scale, when the temperature is lower (Figure 14b) the vaporization rate is faster in the case of pure diesel droplets compared to the blended fuels. This is because RME vapor pressure at lower temperatures is significantly lower than diesel but exhibits an exponential increase with increase in temperature, eventually surpassing the vapor pressure of diesel. This is very clearly seen in Figure 14c which shows an

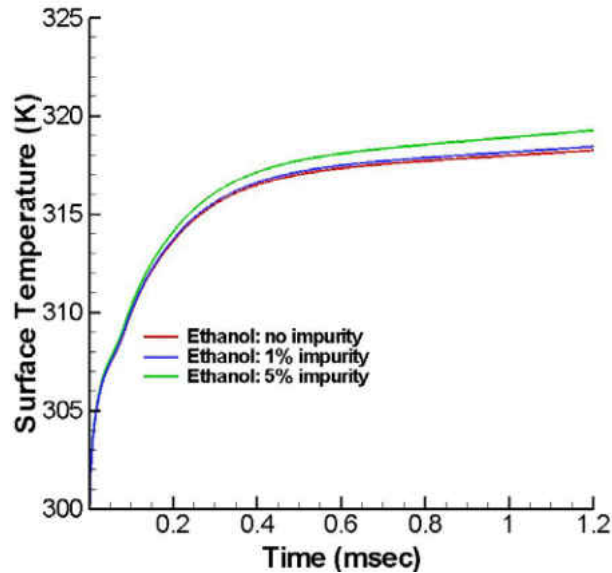
initial increase of RME concentration near the surface followed by a rapid decay signifying that at higher temperatures, RME vaporization rate is faster than diesel.

b) Effect of Knudsen Number

The effect of non-equilibrium (Knudsen number effect) was considered to have some effect on vaporizing droplet. Studies have been conducted by Miller et al [34] to show the effect of nonequilibrium vaporization on different sizes of vaporizing droplets. So it is necessary to study those effects on vaporizing biofuel droplets. However, with current environment of vaporization, no prime change in vaporization pattern was observed. Study was performed for both smaller and larger droplets, which did not show any significant change in diameter reduction or surface temperature rise.



a)



b)

Figure 15: For 20 μm ethanol droplets with different impurity level a) diameter (D_0 is initial diameter, 20 μm) and b) surface temperature (in K) variation

c) Effect of non volatile impurities

Current work also looks into the effect of non-volatile impurities present in biofuels. The non volatile impurities can be thought of as solute in the solvent of pure fuels. During vaporization the solvent part (that is the fuel part) will vaporize, while the solute part or the impurities will get concentrated. As the vaporization of the fuel occurs at the surface, the impurity concentration will start increasing near the surface. It can be inferred that when local concentration of impurities reaches some super saturation limit, it can precipitate. Thus, the presence of impurities can cause problems in fuel injection systems. One of the prime non-volatile impurities generally found in bio-alcohol based fuels is aluminum hydroxide hexa-hydrate ($\text{Al}(\text{OH})_3 \cdot 6\text{H}_2\text{O}$). In this

work, the effect of aluminum hydroxide in pure ethanol droplet vaporization has been studied for 20 μm diameter ethanol droplets. The percentage of impurities present in the fuel varies with the source and extraction process. Two different percentages (1% and 5%) of impurities has been considered for current work.

Figure 15 shows diameter reduction and surface temperature variation with time for 20 micron ethanol droplets with 0% (pure), 1 % and 5 % impurities. It can be noted that in Figure 15a all the three curves are almost similar, which implies that the change in vaporization rate is minimal. A zoomed view and raw-data analysis show that the diameter reduction is slower if impurities are present. In essence, higher concentration of impurities results in slower vaporization rate. But with the current droplet size and percentage of impurities, these variations are very small. This is due to the fact that presence of non-volatile component reduces the vaporization potential of the volatile component. Equation 13 reveals that the mass vaporization rate depends on $B_{M\text{-global}}$, which depends on surface mass fraction of the volatile component(s) as shown in equation 12. The presence of impurities reduces the mass fraction of ethanol which is the volatile component. Slower vaporization rate has some effect on surface temperature as visible in Figure 15b. Considering the same amount of heat transfer from the environment to the droplet, slower vaporization rate involves lower amount of latent heat, increasing the amount of sensible heat which increases the temperature of the droplet. Since the presence of impurities slows down the vaporization rate, it also increases the temperature of the droplet as shown in Figure 15b.

d) Effect of hot and cold zones in pre-mixer

It has been reported in many studies that it is possible to have some discrete zones in the pre-mixer where local temperature is higher or lower than the bulk temperature of the hot air stream. These pockets of high and low temperatures can occur in pre-mixer arbitrarily. The presence of these local hot and cold zones affects the vaporization of the fuel droplets. In this work, studies are conducted to understand the effect of this hot-cold zone on vaporization characteristics of RME-diesel blends. It is difficult to determine the amount of heat transferred from or to the hot or cold zones compared to the surrounding. There are very few published papers in this area. A patent [35] specifies that temperatures of these zones go high or low by 50 °F. In this work, a series of hot and cold zones are considered in the flow field shown in Figure 2. The locations and temperatures of these zones are shown in figure 16.

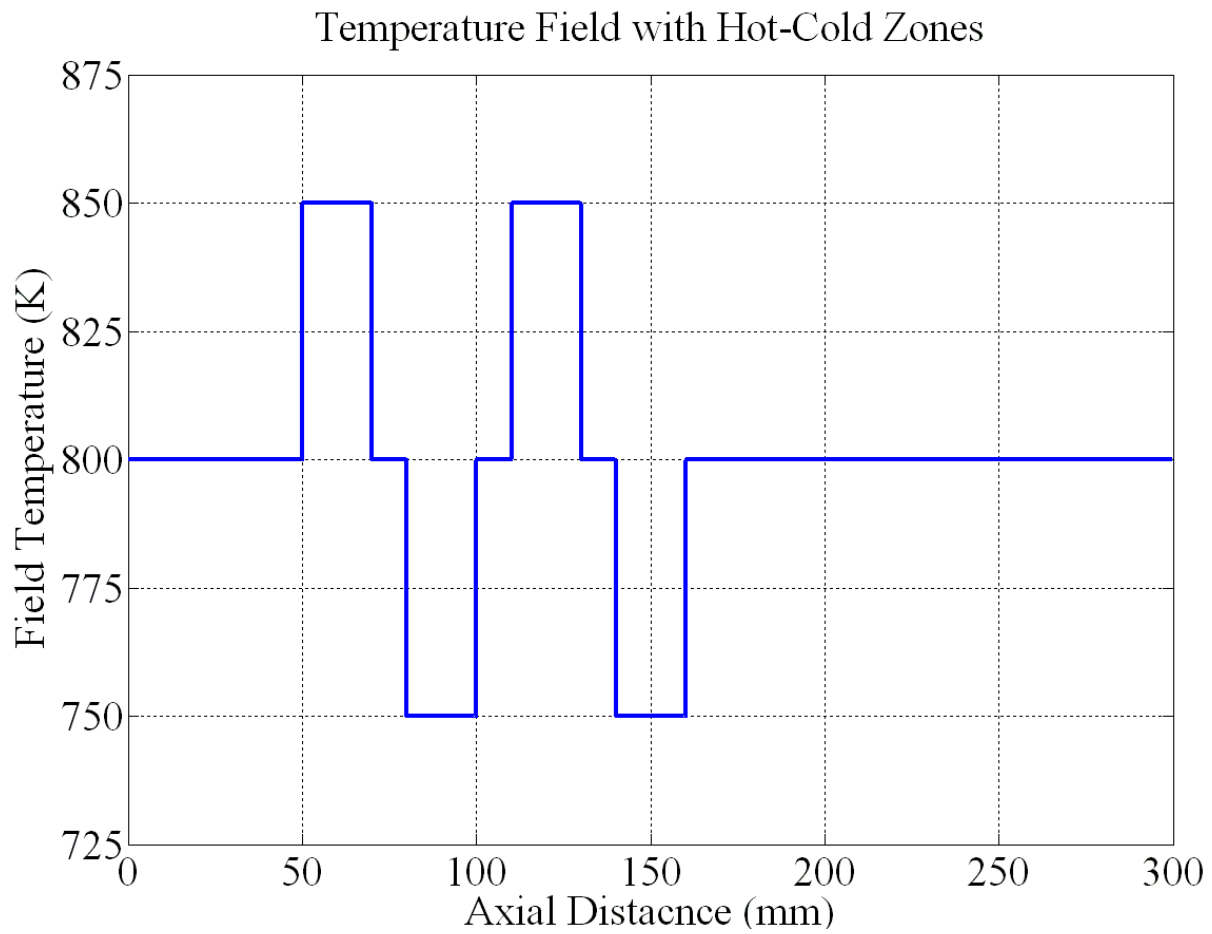


Figure 16: location and temperature of the hot and cold zones used for current work

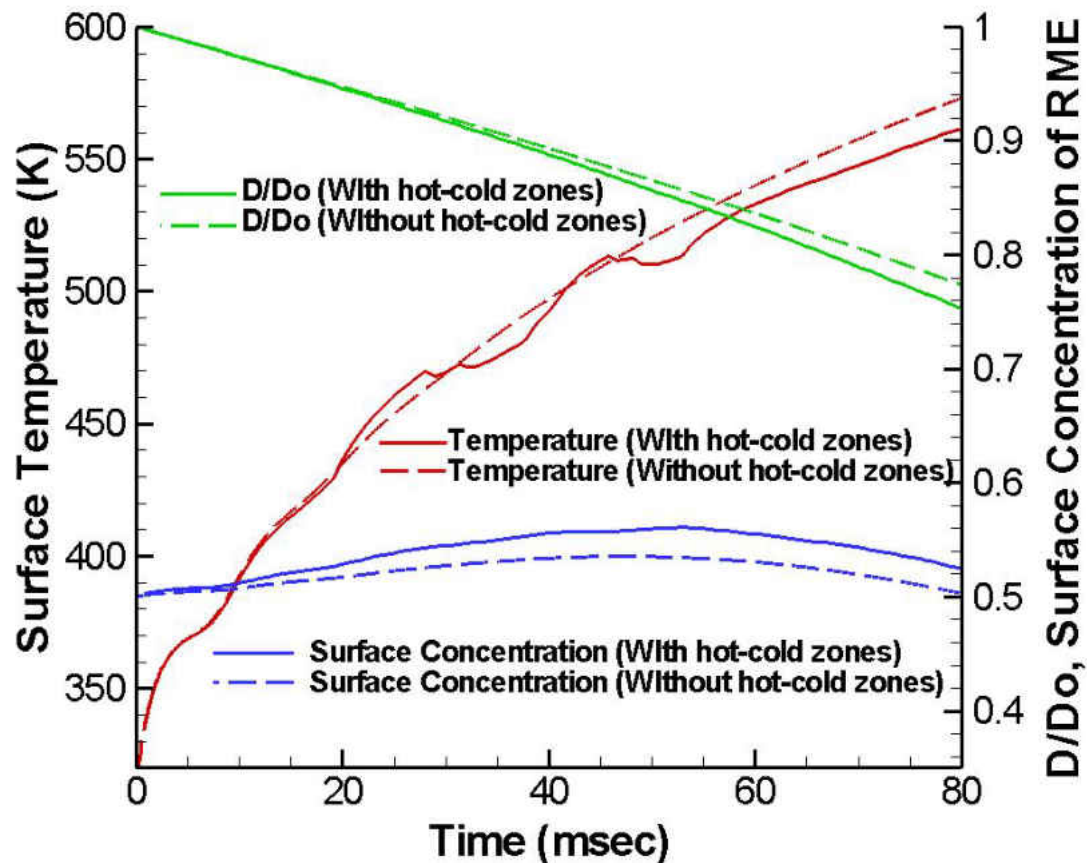


Figure 17: Variation of surface Temperature, Diametric reduction (D/D_o) and surface concentration of RME for a $400\ \mu\text{m}$ RME-diesel (50-50) droplet with the presence of hot-cold zones and without hot-cold zones (base-line).

For a $400\ \mu\text{m}$ RME-Diesel (50-50) droplet, vaporization patterns are studied in the presence of hot and cold zones and then the results are compared to the case in the presence of these hot-cold zones. Figure 17 shows comparative results for these two cases in terms of droplet diameter reduction, surface temperature and surface concentration development with time. The surface temperature plots shows waviness due to hot and cold temperature zones. It clearly shows some peaks and troughs which indicate that the local temperature variation has some effect on the

temperature of the droplet. The surface concentration of RME is also found to be increasing faster than the base case (no hot/cold spots). In Figure 17, it is noted that the temperature deviates from the baseline case, shown as dotted line, at a time instance of 20 msec. It has also been observed that of the first hot spot results in a temperature peak value of 470 K, while for the baseline case, at same time instant, the temperature is ~ 460 K. Referring to the vapor pressures shown in Figure 2, it can be noted that due to the increase in temperature, vapor pressure of diesel goes up from 5.7 kPa to 6.3 kPa, while the vapor pressure of RME goes from 0.42 kPa to 0.64 kPa. Thus, the vapor pressure of both the species has increased, which allows both species to vaporize faster than the baseline case. In addition, the rate of diameter reduction is faster for this blend than the baseline case. It is also noticeable that even though for both cases, the vapor pressure has increased in both species, the increment is higher in the case of diesel droplets. That is why increment in vaporization rate for diesel becomes higher than that of RME. Thus, initial increase in RME concentration at the surface is higher than the baseline case. However, as discussed in the previous sections, the vaporization rate of RME surpasses diesel at higher temperatures. The effect of hot-cold zones has been studied for other blends as well. However, they were observed to repeat the trend discussed here. Thus, it is seen that the characteristics of vaporization are dependent on the location and of hot-cold zone temperatures. For a different position and orientation of hot-cold zone, a different vaporization pattern would result.

CHAPTER FIVE: CONCLUSION

In this work, a numerical model has been developed to study the vaporization characteristics of different blended biofuels. The vaporization pattern and resulting mixing quality are highly dependent on the droplet size and fuel properties. Experiments with acoustically levitated droplet using IR thermography showed very similar trends of volumetric reduction and temperature rise for different fuel types as predicted by the model. This shows that acoustic streaming is an effective way to evaluate vaporization characteristics without any wall effects.

Smaller droplets vaporize faster than larger droplets ensuring homogenous mixture. The 20 μm droplets of ethanol-gasoline 50-50 blend is completely evaporated in 1.1 msec, while 400 μm droplets vaporized only 65% in 80 msec. The results also showed that in gasoline-ethanol blends, pure gasoline is more volatile than pure ethanol. In spite of having higher vapor pressure, ethanol vaporizes slowly compared to gasoline, due to the fact that latent heat of vaporization is higher for ethanol. For gasoline-ethanol blended fuels, ethanol component vaporizes faster. This is because in blended fuels gasoline and ethanol attain the same temperature and for any given temperature, ethanol vapor pressure is higher than gasoline.

In the case of RME-diesel blends, initially diesel vaporizes faster up to 550K, and above this temperature, vapor pressure of RME becomes dominant resulting in faster vaporization of RME. The presence of non-volatile impurities reduces the vaporization rate by reducing the mass fraction of the volatile component at the surface. However, impurities also increase the surface temperature of the droplet.

The presence of non-volatile impurities reduces the vaporization rate by reducing mass fraction of volatile component from the surface. However impurities increase surface temperature of the droplet by reducing the required latent heat of vaporization. Current study further reveals that the presence of hot-cold zones in the pre-mixer changes the vaporization pattern. However, the change depends on the temperature and orientation of these hot-cold zones.

Finally, the experiments with acoustically levitated droplet showed very similar trends of volumetric reduction and temperature rise for different fuel droplets as predicted by the model. This proves that the effect of acoustic streaming and blowing effect can be neglected in the current experiment. The similarity of experimental and numerical results also proves the validity of the model proposed in this work.

In the near future an extensive experimentation with laser induced fluorescence will be performed to study blended biofuel vaporization. The concentration gradient, which is important to quantify Marangoni convection within the droplet, can be estimated using LIF.

REFERENCES

- [1] F.V. Tinaut, Performance of vegetable derived fuels in diesel engine vehicles. Silniki Spanilowe, No. 2/2005, 2005, p. 121
- [2] G.M. Faeth, Evaporation and combustion of sprays, Prog Energy Combust Sci **9** (1983), pp. 1–76
- [3] G.M. Faeth, Mixing, transport and combustion in sprays, Prog Energy Combust Sci **13** (1987), pp. 293–345
- [4] G. M. Faeth Spray combustion phenomena. In: Twenty-sixth symposium (international) on combustion, The Combustion Institute, 1996, p. 1593–612
- [5] G.A.E. Godsave, Studies of the combustion of drops in a fuel spray—the burning of single drops of fuel, Fourth symposium (international) on combustion, Williams & Wilkins, Baltimore (1953), pp. 818–830
- [6] D.B. Spalding, The combustion of liquid fuels, Fourth symposium (international) on combustion, Williams & Wilkins, Baltimore (1953), pp. 847–864
- [7] A. Williams, Combustion of droplets of liquid fuels, a review, Combust Flame **21** (1973), pp. 1–31
- [8] G.M. Faeth, Current status of droplet and liquid combustion, Prog Energy Combust Sci **3** (1977), pp. 191–224

- [9] C.K. Law, Recent advances in droplet vaporization and combustion, *Prog Energy Combust Sci* **8** (1982), pp. 171–201
- [10] A.H. Lefebvre, *Atomization and sprays*, Hemisphere Pub. Co., New York (1989)
- [11] W.A. Sirignano, Theory of multi-component fuel droplet vaporization, *Arch Thermodynamics Combust* **9** (2) (1978), pp. 231–247
- [12] B. Abramzon and W.A. Sirignano, Droplet vaporization model for spray combustion calculations, *Int J Heat Mass Transfer* **12** (9) (1989), pp. 1605–1648.
- [13] A. Berlemont, M.S. Grancher and G. Gouebet, Heat and mass transfer coupling between vaporizing droplets and turbulence using a Lagrangian approach, *Int J Heat Mass Transfer* **38** (17) (1995), pp. 3023–3034
- [14] M. Sommerfeld and H.H. Qiu, Experimental studies of spray evaporation in turbulent flow, *Int. J. Heat Fluid Flow* **19** (1998), pp. 10–22.
- [15] C.X. Bai, H. Rusche and A.D. Gosman, Modeling of gasoline spray impingement, *Atomization Sprays* **12** (2002), pp. 1–27
- [16] J. Barata, Modelling of biofuel droplets dispersion and evaporation, *Renewable Energy* **33** (4), April 2008, pp 769-779
- [17] C. Maqua, G. Castaneta, F. Grisch, F. Lemoine, T. Kristiyadi and S.S. Sazhin, Monodisperse droplet heating and evaporation: Experimental study and modeling, *Int J Heat Mass Transfer* **51** (15-16) (2008), pp. 3932-3945

- [18] G. Castanet, P. Lavieille, F. Lemoine, M. Lebouché, A. Atthasit, Y. Biscos and G. Lavergne, Energetic budget on an evaporating monodisperse droplet stream using combined optical methods: Evaluation of the convective heat transfer, *Int J Heat Mass Transfer* **45** (25) (2002), pp. 5053-5067
- [19] C. Maqua, G. Castanet and F. Lemoine, Bicomponent droplets evaporation: Temperature measurements and modeling, *Fuel* **87**, (13-14), October 2008, pp 2932-2942
- [20] W A Sirignano, Fluid dynamics and transport of droplets and sprays, Cambridge University press (1999).
- [21] M.C. Yuen and L.W. Chen, On drag of evaporating liquid droplet, *Combust. Sci. Technol.* **14** (1976), pp. 147–154.
- [22] G.L. Hubbard, V.E. Denny and A.F. Mills, *Int J Heat Mass Transfer* **16** (1973), pp. 1003–1008
- [23] R Clift, J R Grace and M E Weber, *Bubbles Drops and Particles*, Academic Press, New York(1978)
- [24] A. Ozturk, B.M. Cetegen, Modeling of Plasma Assisted Formation of Yttria Stabilized Zirconia From Liquid Precursors, *Mater. Sci. Eng. A*, 384, 2004 331-351
- [25] G.J. Van Wylen and R.E. Sonntag, *Fundamentals of Classical Thermodynamics*, Wiley (1986).

- [26] M. Renksizbulut and M.C. Yuen, Numerical Study of Droplet Evaporation in a High-Temperature Stream, *J. Heat Trans.* **105** (1983), pp. 389–39
- [27] H. Lamb, *Hydrodynamics*, Cambridge University Press, New York (1993).
- [28] Nist's Chemistry web book.
- [29] M. A. Bremson, *Infrared radiation: A handbook for applications*, Plenum Press, New York (1968)
- [30] W.I. Wolfe, G.J. Zissis, *The infrared handbook*, Office of Naval Research, Department of Navy, Washington DC.
- [31] A.L. Yarin, G. Brenn, O. Kastner, D. Rensink, C. Tropea, Evaporation of acoustically levitated droplets, *J. Fluid Mech.* **399**, 1999, pp 151-204
- [32] M. Seaver, A Galloway and T J Manuccia, Acoustic Levitation in a Free-Jet Wind Tunne, *Rev. Sci. Instrum.*, **60** (1989), 3452
- [33] Y. Tian, G.R. Holt and R.E. Apfel, A new method for measuring liquid surface tension. *Rev. Sci. Instrum.* **56** (1995), pp. 2059–2065
- [34]. Miller R S, Harstad K and Bellan J, *Int J Multiphase Flow* 24(6) (1998), pp 1025-1055
- [35] Smith B C, Anders G A, Patent number: 4188782 (1977), US clasificaton: 60733